Keskinen, Karri; Koch, Jann; Wright, Yuri M.; Schmitt, Martin; Nuutinen, Mika; Kaario, Ossi; Vuorinen, Ville; Larmi, Martti; Boulouchos, Konstantinos

# Numerical assessment of wall modelling approaches in scale-resolving in-cylinder simulations

*Published in:*
International Journal of Heat and Fluid Flow

*DOI:*
10.1016/j.ijheatfluidflow.2018.09.016

Published: 01/12/2018

*Document Version*
Peer-reviewed accepted author manuscript, also known as Final accepted manuscript or Post-print



*Please cite the original version:*
Keskinen, K., Koch, J., Wright, Y. M., Schmitt, M., Nuutinen, M., Kaario, O., Vuorinen, V., Larmi, M., & Boulouchos, K. (2018). Numerical assessment of wall modelling approaches in scale-resolving in-cylinder simulations. *International Journal of Heat and Fluid Flow*, *74*, 154-172.
https://doi.org/10.1016/j.ijheatfluidflow.2018.09.016

# Numerical assessment of wall modelling approaches in scale-resolving in-cylinder simulations

Karri Keskinen[a,*], Jann Koch[b], Yuri M. Wright[b], Martin Schmitt[b,1], Mika Nuutinen[a,2], Ossi Kaario[a], Ville Vuorinen[a], Martti Larmi[a], Konstantinos Boulouchos[b]

[a] *Aalto University School of Engineering*
*Department of Mechanical Engineering*
*Thermodynamics and Combustion Technology Research Group*
*Puumiehenkuja 5 A, 02150 Espoo, Finland*
[b] *ETH Zurich*
*Institute of Energy Technology*
*Aerothermochemistry and Combustion Systems Laboratory*
*ML J40, Sonneggstrasse 3, CH-8092 Zurich, Switzerland*

**Abstract**

Wall modelling in internal combustion engines (ICEs) is a challenging task due to highly specific boundary layers and a dynamically changing flow environment. Recent experimental (Jainski et al., 2013; Renaud et al., 2018) and direct numerical simulation (DNS, Schmitt et al., 2015a) studies demonstrate that scaled near-wall velocity and temperature profiles in ICEs deviate considerably from the law of the wall. Utilising the DNS data, the present paper focusses on benchmarking a scale-resolving approach with a 1-D non-equilibrium wall model (HLR-WT, Keskinen et al., 2017) in ICE-like flows. Specific emphasis is put on the compression stroke using different grids and two additional wall-modelled large eddy simulation (WMLES) reference approaches. The standard wall law based WMLES-1 produces highly grid-dependent underprediction of wall fluxes, to which WMLES-2 (Plensgaard and Rutland, 2013) and HLR-WT, employing engine-targeted wall treatments, yield considerable improvement. Differences between the improved methods are noted in detailed metrics. Throughout the compression stroke, HLR-WT provides a good match to the DNS in scaled mean boundary layer profiles for both velocity and temperature. With relevance to local heat flux distribution, the characteristic impingement-ejection process observed in the DNS

*Corresponding author. Tel.: +358 50 409 4217
*Email address:* `karri.keskinen@aalto.fi` (Karri Keskinen)
[1]Present address: Robert Bosch GmbH, Schwieberdingen, Germany
[2]Present address: ABB Oy, Marine and Ports, Merenkulkijankatu 1, 00980 Helsinki, Finland

is qualitatively replicated with WMLES-2 and HLR-WT. The non-equilibrium formulation of the latter allows for slight improvements in terms of local heat transfer fluctuation predictions. In contrast, coarse near-wall grids appear to be detrimental for such predictions with all approaches. The study provides evidence on the potential of the HLR-WT and WMLES-2 approaches in ICE near-wall flow prediction, advocating further investigations in more realistic engine configurations.

*Keywords:* Wall modelling, Wall-modelled large eddy simulation, Engine flows, Compression stroke, Wall heat transfer

---

## 1. Introduction

### 1.1. Background

Near-wall fluid flow processes and wall heat transfer have a substantial influence on internal combustion engine (ICE) charge conditions such as temperature and flow turbulence. With the concurrent prospect of high thermal efficiency and low emissions, ICE research and development is increasingly focussed on modern, sensitive concepts such as lean combustion, homogeneous charge compression ignition (HCCI) or reactivity controlled compression ignition (RCCI) (Reitz, 2013). Hence, the understanding and predictive analysis of such modern concepts benefits from the comprehension and accurate prediction of near-wall processes.

Modern computational methods (direct numerical simulation, DNS; large eddy simulation, LES) aim at the description of temporally and spatially resolved turbulent flow fields and associated flow processes such as heat transfer and combustion. For DNS (depicting all turbulent scales), computational time dependence on pressure $p$, rotational speed $n$ and stroke $S$ scales with $p^3n^3S^6$ in ICE simulations (Frouzakis et al., 2017), leading to remarkable increases for large supercharged engines operated at high speeds. Although DNS will likely remain prohibitively expensive for engineering simulations in the near future (particularly if multi-cycle statistics are required), LES (resolving turbulent scales larger than a filtering threshold) has gained a firm standing as a complement to the widespread Reynolds-averaged (RANS) technique.

However, wall boundary layers pose a considerable challenge to LES (cf. Pope, 2004): for accurate predictions of near-wall turbulence and heat transfer, near-wall grid resolution is required to approach DNS standards. In ICEs, LES quality has been discussed by di Mare et al. (2014) who present, among other metrics, the popular estimators based on modelled turbulent kinetic energy and modelled viscosity. However, conventional near-wall metrics such as scaled tangential resolution are less frequently studied. Considering the complexity of ICE flows, it may not be straightforward to adopt near-wall criteria established for flat-plate boundary layers (e.g. Choi and Moin, 2012). In fact, in-cylinder wall-resolved LES investigations are scarce and unaffordable computational costs are associated with high Reynolds numbers and complex engine configurations (Misdariis et al., 2015).

Wall-modelled LES (WMLES; referring here to wall stress models) and hybrid LES/RANS methods (cf. (Larsson et al., 2016) for taxonomic perspectives) represent some of the primary avenues for alleviation of the near-wall issue (see reviews of Piomelli, 2008; Sagaut et al., 2013; Larsson et al., 2016; Chaouat, 2017). Interest in such scale-resolving methods has also been raised within the engine research community (Hasse, 2016). However, knowledge of the functionality of different approaches is not extensive in the ICE context, where wall modelling advances are not frequent and clear research gaps have been previously identified (Rutland, 2011). Many groups have applied models based on the law of the wall or closely related correlations (e.g. Vermorel et al., 2009; Enaux et al., 2011; Misdariis et al., 2015; Truffin et al., 2015; Schiffmann et al., 2016) while engine-targeted algebraic models have also been adapted for WMLES (Plensgaard and Rutland, 2013). Conversely, some contemporary studies consciously disregard wall treatment (in favour of straightforward linear gradient approximations), stating either modelling difficulty (Nguyen et al., 2016) or the known departures from typical wall law (equilibrium) assumptions (He et al., 2017). In general, near-wall flows or wall heat transfer are only rarely a focal component of ICE-related LES papers.

In-cylinder flows differ considerably from channel or pipe flows, wherein the law of the wall, for both wall shear stress and convective heat transfer, can often be considered to be an acceptable approximation (White, 2006). As revealed by particle image velocimetry (PIV) measurements (Jainski et al., 2013) and DNS (Schmitt et al., 2015a), scaled near-wall velocity and temperature profiles in ICEs deviate from the law of the wall substantially. Such variations are also influenced by engine operating conditions (Renaud et al., 2018) or local flow regions dominated by (i) wall-parallel and (ii) stagnating contributions (Buhl et al., 2017b). Renaud et al. (2018) found near-wall velocity profiles to resemble accelerated boundary layers following impingement. Such an impinging flow type is well-known for local variation of scaled profiles (Hattori and Nagano, 2004). ICE wall models should hence be applicable to many types of flows in highly dynamic in-cylinder conditions. For RANS, improved wall models accounting for considerable near-wall material property variations were introduced by Han and Reitz (1997) and Angelberger et al. (1997). Later on, further advances have been made in complex flows (e.g. Craft et al., 2002; Popovac and Hanjalic, 2007; Suga et al., 2013; Nuutinen et al., 2014). Non-equilibrium models have recently been advocated in experimentally based ICE near-wall layer investigations (Ma et al., 2017a,b) and have become a frequent topic in recent WMLES studies not specifically pertaining to engines (Kawai and Larsson, 2013; Park and Moin, 2014; Yang et al., 2015).

### *1.2. Study objectives*

Based on the literature survey, there is a research gap in wall modelling for scale-resolving ICE simulations. The recent DNS work on engine-like flows (Schmitt et al., 2014a,b, 2015a,b, 2016a,b; Schmitt and Boulouchos, 2016) provides a unique opportunity to benchmark various approaches. Here, existing methods are assessed by implementing algebraic WMLES methodologies based on standard wall laws (WMLES-1) and engine-targeted models (WMLES-2). In addition, an approach with a non-equilibrium wall model aimed at ICE flows (HLR-WT), recently investigated in canonical flows (Keskinen et al., 2017), is further assessed here. Simulations comprise three consecutive stages: (I) cold, multi-cycle reciprocating flow, (II) fuel-air intake, and (III) charge compression, while stage III is the main focus of the present work. The objectives of this study are stated as follows:

1. Comparing with the DNS data, assess the predictive ability of the approaches in terms of mean quantities such as global wall heat transfer.
2. Examine how the specific near-wall profiles found in the DNS are reproduced with the

methods.

3. Analyse how focal physical near-wall mechanisms observed in the reference results are replicated in the present simulations.
4. Investigate result sensitivity to grid variations both in the core flow and in the near-wall region.

The paper is structured so that turbulence modelling and near-wall methodologies are presented in Sec. 2, while the present engine-like test case setting and utilised computational grids are reported in Sec. 2.7. Results in Sec. 3 convey a brief overview of stages I to III followed by volume-averaged quantities in the compression stroke. Observations are then gradually taken to a more detailed level, highlighting approach and grid-specific differences not easily evidenced through averaged metrics. Finally, a discussion attempts to convey relevant practical aspects to the investigation.

## 2. Methodology

### *2.1. Governing equations*

The present simulations consist of three stages (I-III) explained in detail in Sec. 2.7. While stage I is based on an incompressible formulation (see Keskinen et al., 2017), we next explain the methodology used herein for the compressible intake (II) and compression (III) processes. The simulations provide numerical solutions to the filtered compressible mass, momentum, energy and species transport equations. Utilising density-weighted $(\tilde{\cdot})$ and non-density-weighted $(\hat{\cdot})$ filtering notations, the governing equations read in Cartesian coordinates with the Einstein notation:

$$\frac{\partial \hat{\rho}}{\partial t} + \frac{\partial (\hat{\rho}\tilde{u}_j)}{\partial x_j} = 0 \tag{1}$$

$$\frac{\partial (\hat{\rho}\tilde{u}_i)}{\partial t} + \frac{\partial (\hat{\rho}\tilde{u}_j\tilde{u}_i)}{\partial x_j} = -\frac{\partial \hat{p}}{\partial x_i} + \frac{\partial \hat{\tau}_{ij}}{\partial x_j} - \frac{\partial \tau^r_{ij}}{\partial x_j} \tag{2}$$

$$\frac{\partial (\hat{\rho}\tilde{h})}{\partial t} + \frac{\partial (\hat{\rho}\tilde{u}_j\tilde{h})}{\partial x_j} = \frac{\partial \hat{p}}{\partial t} - \frac{\partial}{\partial x_j}\left(\hat{q}_j + q^r_j\right) + \tilde{u}_j\frac{\partial \hat{p}}{\partial x_j} + \left(\hat{\tau}_{ij} + \tau^r_{ij}\right)\frac{\partial \tilde{u}_i}{\partial x_j} \tag{3}$$

$$\frac{\partial (\hat{\rho}\tilde{Y}_m)}{\partial t} + \frac{\partial (\hat{\rho}\tilde{u}_j\tilde{Y}_m)}{\partial x_j} = -\frac{\partial}{\partial x_j}\left(\hat{f}_{j,m} + f^r_{j,m}\right) \tag{4}$$

where $\hat{\rho}$, $\tilde{u}$, $\hat{p}$, $\tilde{h}$ and $\tilde{Y}_m$ refer to density, velocity, pressure, static enthalpy and species mass fraction, respectively, whereas quantities $\hat{\tau}_{ij}$, $\hat{q}_j$ and $\hat{f}_j$ respectively correspond to the viscous stress tensor, heat flux vector and species flux vector. Unresolved (residual) quantities are modelled in the residual stress tensor $\tau_{ij}^r$, residual heat flux vector $q_j^r$ and residual species flux vector $f_j^r$, expressed here with an eddy-viscosity model

$$\tau_{ij}^r = \hat{\rho}\left(\widetilde{u_j u_i} - \tilde{u}_j \tilde{u}_i\right) = -2\mu_{mod}\tilde{S}_{ij}^d + \frac{2}{3}\delta_{ij}\left(\mu_{mod}\frac{\partial \tilde{u}_k}{\partial x_k} + \rho k_{mod}\right) \tag{5}$$

$$q_j^r = \hat{\rho}\left(\widetilde{u_j h} - \tilde{u}_j \tilde{h}\right) = -\frac{\mu_{mod}}{\mathrm{Pr}_{mod}}\frac{\partial \tilde{T}}{\partial x_j} \tag{6}$$

$$f_{j,m}^r = \hat{\rho}\left(\widetilde{u_j Y_m} - \tilde{u}_j \tilde{Y}_m\right) = -\frac{\mu_{mod}}{\mathrm{Sc}_{mod}}\frac{\partial \tilde{Y}_m}{\partial x_j} \tag{7}$$

where $\mu_{mod}$ is modelled viscosity, $\tilde{S}_{ij}^d$ is the traceless deviator of the resolved strain rate tensor $\tilde{S}_{ij} = 0.5\left(\partial \tilde{u}_i/\partial x_j + \partial \tilde{u}_j/\partial x_i\right)$, $\tilde{T}$ is temperature, $k_{mod}$ is modelled turbulent kinetic energy, $\mathrm{Pr}_{mod}$ is the modelled Prandtl number and $\mathrm{Sc}_{mod}$ is the modelled Schmidt number. Gases in this study are considered ideal.

### 2.2. LES model

For WMLES and the LES zone of hybrid LES/RANS simulations, modelled viscosity $\mu_{mod}$ equals $\mu_{sgs}$ determined according to the $\sigma$-model by Nicoud et al. (2011):

$$\mu_{sgs} = \hat{\rho}\left(C_\sigma \Delta\right)^2 \frac{\sigma_3(\sigma_1 - \sigma_2)(\sigma_2 - \sigma_3)}{\sigma_1^2} \tag{8}$$

where $C_\sigma = 1.35$ is a model constant, $\Delta = V_{cell}^{1/3}$ is the filter width where $V_{cell}$ is cell volume, and $\sigma_1 \geq \sigma_2 \geq \sigma_3 \geq 0$ are singular values of the resolved velocity gradient tensor $\partial \tilde{u}_i/\partial x_j$. The $\sigma$-model is an explicit subgrid-scale (SGS) model without transport equations or dynamic filtering. SGS contributions vanish in many physically justified scenarios and cubic asymptotic behaviour is satisfied near solid walls. The model has been extensively validated and used in various previous studies with simple geometries (e.g. Toda et al., 2014; Rieth et al., 2014). High model suitability for engine-like flows was noted in the recent investigation of Buhl et al. (2017a). Here, SGS kinetic energy and dissipation rate are estimated in analogy to a model proposed by Mason and Callen (1986) for the Smagorinsky model:

$$k_{sgs} = \nu_{sgs}^2/(C_s^2\Delta^2 C_\mu^{1/2}) \tag{9}$$

$$\varepsilon_{sgs} = \nu_{sgs}^3/(C_s\Delta)^4 \tag{10}$$

where $\nu_{sgs} = \mu_{sgs}/\hat{\rho}$, $C_s = 0.165$ and $C_\mu = 0.09$. For Eqs. (6) and (7), the modelled Prandtl and Schmidt numbers $\mathrm{Pr}_{mod} = \mathrm{Sc}_{mod} = 0.9$. Justified deviations in $\mathrm{Pr}_{mod}$ were noted to have little influence on the results of this study, likely due to limited extent of modelled turbulence.

### *2.3. Reference wall models*

Two engine research-relevant algebraic WMLES-models are considered in this work. WMLES-1 combines a linear-power law for wall shear stress (Werner and Wengle, 1991) with a linear-log law for wall heat flux:

$$u^+ = \begin{cases} y^+, & y^+ \leq 11.81 \\ A(y^+)^B, & y^+ > 11.81 \end{cases} \tag{11}$$

$$T^+ = \begin{cases} \mathrm{Pr}\ y^+ & y^+ \leq 5 \\ \min\left(\mathrm{Pr}\ y^+, \kappa^{-1}\ln\left[C_T y^+\right]\right) & y^+ > 5 \end{cases} \tag{12}$$

where $A = 8.3$, $B = 1/7$, $C_T = 2.96$ and $u$ denotes the wall-relative tangential velocity. Variable scaling follows $y^+ = \rho_w u_\tau y/\mu_w$, $u^+ = (u_c - u_w)/u_\tau$, $T^+ = \rho_w u_\tau c_{p,w}(T_w - T_c)/q_w$ where $u_\tau = (\tau_w/\rho_w)^{1/2}$ and subscripts $c$ and $w$ denote cell and wall values, respectively. The Werner-Wengle model, applied by e.g. Schiffmann et al. (2016), is functionally very similar to the two-layer linear-log law for velocity. Schmitt et al. (2007) first applied the logarithmic part of Eq. (12) with a log-law for velocity in a burner WMLES, and their model has been used in several ICE WMLES studies (Vermorel et al., 2009; Enaux et al., 2011; Misdariis et al., 2015).

Plensgaard and Rutland (2013) developed a formulation entailing an improved Werner-Wengle model (including an SGS contribution) and a modified heat flux approach based on the engine-targeted model of Han and Reitz (1997) (herewith, WMLES-2). The model was tested in duct flows and impinging jets in addition to reacting engine flows (Plensgaard, 2013), and is implemented here as

$$\tau_w = \begin{cases} 2\mu_w u/\Delta y, \quad u \leq \frac{\nu_w}{2\Delta y} A^{2/(1-B)} \\ \rho_w \left[ \frac{1-B}{2} A^{\frac{1+B}{1-B}} (\frac{\nu_w + \nu_{k,c}}{\Delta y})^{1+B} + \frac{1+B}{A} (\frac{\nu_w + \nu_{k,c}}{\Delta y})^{B} u \right]^{2/(1+B)}, \; u > \frac{\nu_w}{2\Delta y} A^{2/(1-B)} \end{cases} \tag{13}$$

$$q_w = \begin{cases} \frac{\rho_w u_\tau c_{p,w} T_c \ln(T_c/T_w)}{c_{hw}[7.483 \arctan(0.0935 y^+)]}, \quad y^+ \leq 40 \\ \frac{\rho_w u_\tau c_{p,w} T_c \ln(T_c/T_w)}{c_{hw}[2.1 \ln(y^+) + 2.5]}, \quad y^+ > 40 \end{cases} \tag{14}$$

where $\Delta y$ is the near-wall cell height. Eq. (13) differs from the original Werner-Wengle law by introducing a modelled viscosity based on the near-wall modelled kinetic energy $\nu_{k,c} = c_{mw} V_{cell}^{0.33} k_{mod,c}$ where $c_{mw} = 0.01$. In contrast to the present method (Eq. 9), the original approach employs a one-equation SGS model in the determination of $k_{mod}$, while model parameters $c_{mw} = 0.01$ and $c_{hw} = 0.8$ were introduced based on square duct flow calibration studies (Plensgaard and Rutland, 2013).

### *2.4. HLR-WT approach*

#### *2.4.1. Hybrid LES/RANS model*

The present zonal approach (HLR) follows the work of Jakirlić et al. (2010) and involves a fixed LES/RANS interface (see (Jakirlić et al., 2011) for a dynamic approach). The RANS zone employs a low-Reynolds $k-\varepsilon$ turbulence model based on the model of Lien et al. (1996) with pertinent modifications detailed in our previous study (Nuutinen et al., 2014). Continuity of modelled viscosity across the nominal LES/RANS interface is implicitly imposed by setting $k_{sgs}$ and $\varepsilon_{sgs}$ (Eqs. (9)-(10)) in the first cell of the LES domain via source terms (cf. (Jakirlić et al., 2011) for a more detailed description). Interfaces in this study are placed manually to a scaled wall-normal distance of $y_1^+ \approx \mathcal{O}(100)$ in maximum gradient conditions, while intake jet regions were set in the LES zone. Variation of this scaled distance ensues due to the transient process. Various interface positions between $\mathcal{O}(50)$-$\mathcal{O}(600)$ have been applied with zonal approaches (e.g. Piomelli et al., 2003; Temmerman et al., 2005; Jakirlić et al., 2011). Based on numerical tests in the present setup (not shown herein for brevity), results were not noted to be very sensitive to the exact position of the interface, corresponding with previous canonical flow observations (Keskinen et al., 2017).

In the HLR approach, Eqs. (1)-(4) incorporate an effective filter width (Jakirlić et al., 2011; Sagaut et al., 2013): in the RANS zone, the model mimics an SGS model whose length scale corresponds to the SGS width at the LES/RANS interface, approaching the scale $l_{RANS} = k^{3/2}/\varepsilon$ close to the wall (Jakirlić et al., 2011). As noted in our previous work (Keskinen et al., 2017), modelled contribution depends on the interface position and on the local flow state. Pure Reynolds-averaged simulation (devoid of any resolved turbulent fluctuations) should not be expected in RANS zones. Furthermore, very low modelled viscosity values were previously noted around near-wall stagnation flow regions. Hence, in the present work, modelled viscosity is limited in nominal RANS zones as $\mu_{mod} = \max(\mu_{sgs}, \mu_{RANS})$ for enhanced computational stability.

### 2.4.2. 1-D non-equilibrium wall model

The wall treatment developed by Nuutinen et al. (2014) in the RANS context is specifically designed for engine-like boundary layers and engine wall heat transfer. The present hybrid LES/RANS implementation was previously benchmarked in incompressible channel and impinging jet flows (Keskinen et al., 2017). Starting from main grid data at two wall-adjacent cell layers, the model solves simplified 1-D turbulent boundary layer equations (TBLEs) for momentum and enthalpy:

$$\frac{d}{dy}\left(\underbrace{[\mu + \mu_{mod}]}_{\mu_{eff}}\frac{du}{dy}\right) = \overbrace{I_m}^{const.} \Rightarrow \quad \frac{du}{dy} = \frac{\overbrace{\tau_w + I_m y}^{\tau(y)}}{\mu_{eff}} \tag{15}$$

$$\frac{d}{dy}\left(\underbrace{c_p\left[\frac{\mu}{Pr} + \frac{\mu_{mod}}{Pr_{mod}}\right]}_{k_{T,eff}}\frac{dT}{dy}\right) = \overbrace{I_h}^{const.} \Rightarrow \quad \frac{dT}{dy} = \frac{\overbrace{q_w + I_h y}^{q(y)}}{k_{T,eff}} \tag{16}$$

where $k_T$ is thermal conductivity. Solution is carried out on an equidistant 1-D subgrid with spacing smaller than one dimensionless wall unit. The central assumption is that the several terms within momentum ($I_m$) and enthalpy ($I_h$) imbalances are not explicitly modelled but their collated profiles are assumed to be independent of $y$ based on observations regarding convection and pressure gradient in backward-facing step and impinging jet flows (Popovac and Hanjalic, 2007). This represents a highly simplified but physically consistent approach in comparison to modelling only some of the terms individually (Larsson et al., 2016). The unknown imbalance term values are formed within the iterative routine, while $\mu_{eff}$ and $k_{T,eff}$ profiles are determined using algebraic simplifications of a linear low-Reynolds $k-\varepsilon$ model (Lien et al., 1996). Temperature-dependent material property variations throughout the subgrid are concisely included in nondimensionalised equations via power law expressions. As a result from converged near-wall profiles, the routine provides wall shear stress and wall heat flux linearisation coefficients as well as modelled turbulence source terms for the main solver. Appendix A provides further details regarding the model.

### *2.5. Wall model discussion*

The common objective of the investigated approaches is to provide accurate wall flux predictions based on information that can be gathered from different components of the main grid solution. Table 1 displays a summary of wall model characteristics such as input and output quantities. Although the 1-D model formulation is much more complicated in comparison to the algebraic models, it is worth recalling that the latter can be considered to represent simplified solution sets for TBLEs where non-equilibrium terms cancel out ($I_m = I_h = 0$). Furthermore, equilibrium models may not be as restrictive as their formulation suggests due to the non-equilibrium effects inherently captured by LES in the outer layer (Larsson et al., 2016). For ICE boundary layers, the straightforward incorporation of material property variations should be considered an advantage of both equilibrium and non-equilibrium 1-D models.

An additional difference between the approaches arises from the sequence in which the output quantities are evaluated. In WMLES-1 and WMLES-2, $\tau_w$ is first determined while the result ($u_\tau$) is fed to the convective heat transfer model, cf. Eqs. (12) and (14). Hence, an explicit link between $\tau_w$ and $q_w$ is constructed in line with the Reynolds analogy, whereof some effects will be discussed in Sec. 3.6. In HLR-WT, Eqs. (15)-(16) are iterated simultaneously while the output quantities are linked only implicitly through material property and modelled

Table 1: Characteristic description of the present wall-modelled approaches. In addition to the listed near-wall (NW) grid point data, all models employ material properties, wall velocity and wall temperature as input.

| | WMLES-1 | WMLES-2 | HLR-WT |
|---|---|---|---|
| Wall model format | algebraic | algebraic | simplified 1-D TBLE |
| Solution method | explicit | explicit | iterative |
| Input data ($\tau_w$) | $u$ | $u, \mu_{mod}$ | $u, T, \mu_{mod}, k_{mod}, \varepsilon_{mod}$ |
| Input data ($q_w$) | T,$u_\tau$ | T,$u_\tau$ | |
| Input data location | first NW grid point | first NW grid point | first and second NW grid points |
| Modelled non-equilibrium | - | - | constant imbalance model |
| Material property variation | - | embedded ($\mu, \rho$) | $\mu, c_p, k_T, \rho$ |
| Output data | $\tau_w, q_w$ | $\tau_w, q_w$ | $\tau_w, q_w$, source terms for $k_{mod}$,$\varepsilon_{mod}$ |

viscosity profiles.

### 2.6. Numerical aspects

Simulations are carried out with the Star-CD v. 4.20 software (licensed by CD-Adapco). The momentum equation is discretised with central differencing whereas for scalar quantities, including modelled turbulence equations, the monotone advection reconstruction scheme (MARS) is employed (CD-Adapco, 2013). The pressure-implicit splitting of operators (PISO) method is utilised for pressure-velocity coupling. Grid resolutions are discussed in stage-specific subsections. The SGS model, hybrid LES/RANS interfacing and wall models of the present work are implemented as user subroutines.

### 2.7. Test cases

Figure 1 shows a general schematic of the case, originating from the experimental flow study of Morse et al. (1979) and further expanded by DNS investigations (Schmitt et al., 2014a,b, 2015a,b, 2016a; Schmitt and Boulouchos, 2016). Here, we divide the present computational tasks into three stages, consistent with the manner in which the DNS results were generated. Preliminary stages I and II aim to (1) benchmark the methodology in a cold engine-like flow, and to (2) generate several bottom dead centre (BDC) conditions for compression stroke simulations, thus permitting the assessment of cycle selection influence.

#### 2.7.1. Stage I: Multiple cold flow cycles

Consecutive cycles of a valve-piston assembly are simulated with a compression ratio of 3:1, containing air at atmospheric conditions, corresponding to the original experiment

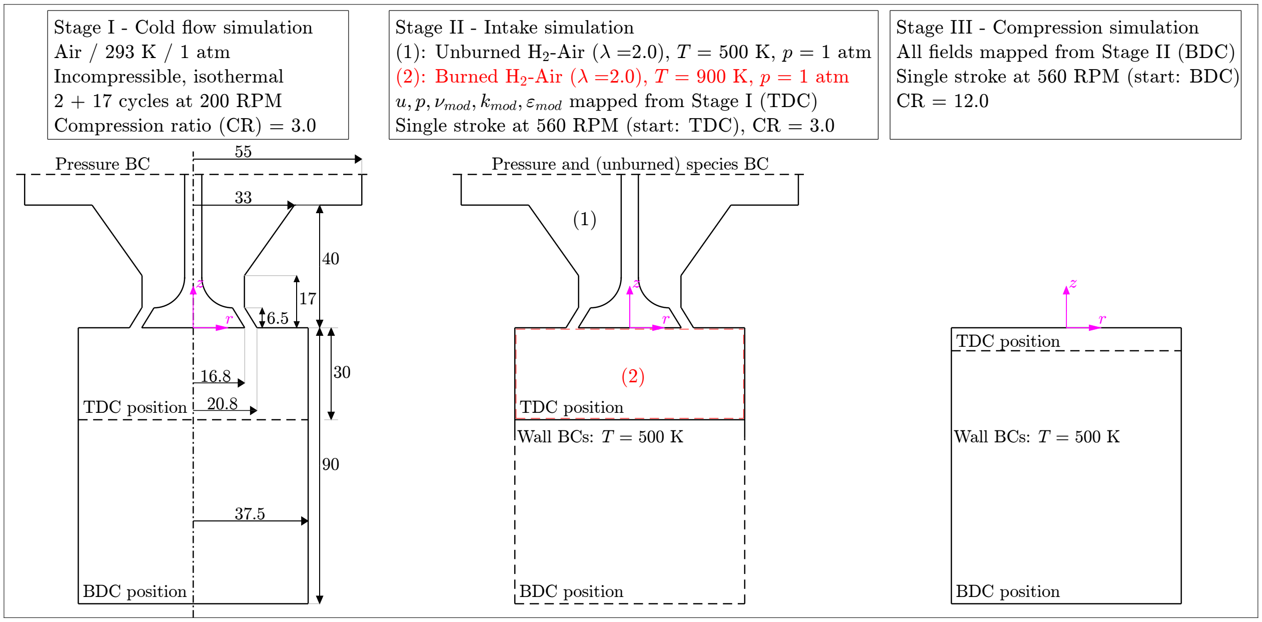


Figure 1: Schematic description of the three simulation types in the present study: consecutive cold flow cycles (stage I), single intake cycle (II) and single compression cycle (III). System dimensions are expressed in millimetres.

(Morse et al., 1979) as well as several computations (e.g. Schmitt et al., 2014b; Keskinen et al., 2015; Montorfano et al., 2015; Buhl et al., 2017a). In contrast to actual engine crank kinematics, piston movement is prescribed by simple sinusoidal motion at a rotational speed of 200 revolutions per minute (RPM). The filtered result quantities are averaged spatially in the azimuthal direction and phase-averaged over the simulated cycles. The DNS and LES studies cited above simulated 6 to 13 consecutive cycles, while the present work includes 17 cycles (in addition to the first two cycles which are disregarded). Stage I and II computations are carried out with a grid containing $2.3 \times 10^6$ hexahedral/polyhedral cells at BDC and $1.1 \times 10^6$ at top dead centre (TDC). This grid count clearly exceeds early LES studies of the case (e.g. Haworth and Jansen, 2000, $N = 0.15 \times 10^6$) but is also lower than contemporary LES investigations (Montorfano et al., 2015; Keskinen et al., 2015; Buhl et al., 2017a, $N = 4.6 \times 10^6$, $N = 5.1 \times 10^6$, $N = 14.5 \times 10^6$, respectively).

### *2.7.2. Stage II: Intake stroke*

The flow field at the end of the preceding cycle was noted by Schmitt et al. (2014a) as an influential factor in the dominant processes of jet development and vortex ring generation. In stage II, an intake stroke is initialised from TDC, maintaining the velocity, pressure

Table 2: Dimensional metrics for stage III compression stroke simulations. Wall-normal ($y_1$) tangential ($\Delta_{tan}$, see Fig. 2), axial ($\Delta_z$) and azimuthal ($R_c\Delta\phi$) spacings are provided here.

| | M1 | M1-CW | M2 | M2-CW | M3 |
|---|---|---|---|---|---|
| Cells (BDC) | $0.44 \times 10^6$ | $0.43 \times 10^6$ | $2.6 \times 10^6$ | $2.4 \times 10^6$ | $6.4 \times 10^6$ |
| Cells (TDC) | $0.65 \times 10^5$ | $0.65 \times 10^5$ | $0.31 \times 10^6$ | $0.24 \times 10^6$ | $0.69 \times 10^6$ |
| $y_1$ (mm) | 0.14 | 0.20 | 0.12 | 0.20 | 0.12 |
| $\Delta_{tan}$ (mm) | 1.2 | 1.2 | 0.59 | 0.59 | 0.44 |
| $\Delta_z$ (mm) | 1.0 | 1.0 | 0.60 | 0.60 | 0.40 |
| $R_c\Delta_\phi$ (mm) | 1.4 | 1.4 | 0.70 | 0.70 | 0.53 |

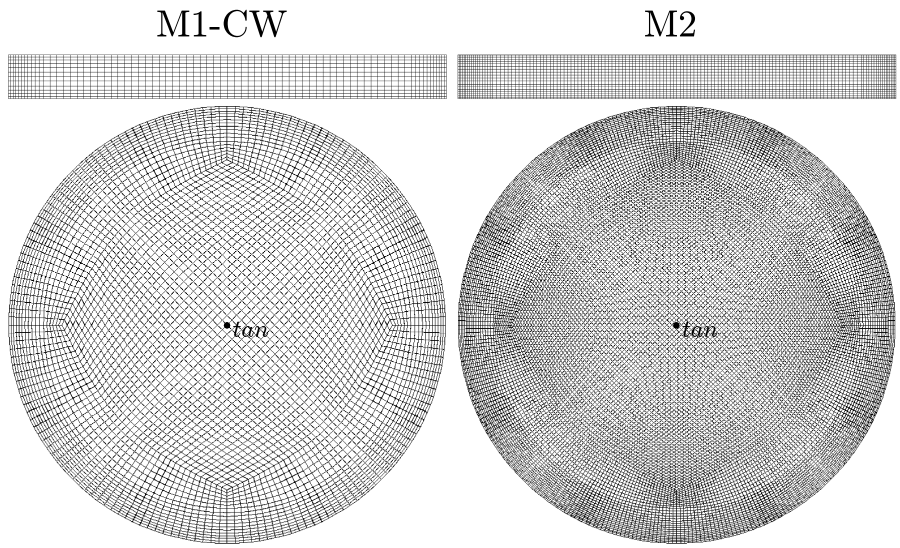


Figure 2: Vertical (top; TDC piston position) and horizontal (bottom) cutouts of grids used in stage III computations. Coarse & coarse-wall (M1-CW; left) and intermediate & nominal-wall (M2; right) variants are shown here. Annotated points in the grid images indicate the measurement location for $\Delta_{\text{tan}}$ in Table 2 and Fig. 3.

and modelled turbulence fields from a selected stage I cycle. A nominal cycle (A) and two differing cycles (B & C) are determined based on azimuthally averaged flow fields (see Appendix B). The following additional considerations reflect the DNS reference (Schmitt et al., 2015a): homogeneous mixtures of burned (in-cylinder) and unburned (intake) gases, based on equilibrium chemistry, are initialised with respective temperatures of 900 K and 500 K. Hydrogen ($H_2$) is employed as the fuel with a relative air-fuel ratio ($\lambda$) of 2.0 compared to stoichiometry. A fixed wall temperature condition of $T_w = 500$ K is set at the walls and the engine speed is set at 560 RPM.

### 2.7.3. *Stage III: Compression stroke*

Stage III is initialised from the BDC result of stage II, while the geometric compression ratio is increased from 3:1 to 12:1 in analogy to the DNS. Three core flow (off-wall) resolutions (M1, M2, M3) and two near-wall resolutions (nominal, coarse-wall [CW]) are considered in order to assess the influence of both grid variation types independently. Table 2 provides basic dimensional metrics for the different grids (shown in Fig. 2), while Fig. 3 illustrates how the highly dynamic compression stroke influences dimensionless metrics. The first wall-normal grid points are set to locations that eventually exceed the viscous sublayer and are thus interesting from the wall modelling perspective. The locations are also within the boundary layer thickness: in Fig. 3, $\delta_{90,t}$ represents the wall-normal distance at which the mean temperature gradient has decreased by 90% in comparison to its maximum value. This differs from the classical definition due to the time-dependent mean flow outside the boundary layer (Schmitt et al., 2015a). The reference DNS grid initialises at $90 \times 10^6$ nodes and is refined at 306°CA after top dead centre (ATDC) to $135 \times 10^6$ nodes (Schmitt et al., 2015a). The present computations are carried out without intermittent refinement while cell layer removal is employed to maintain a near-constant axial resolution.

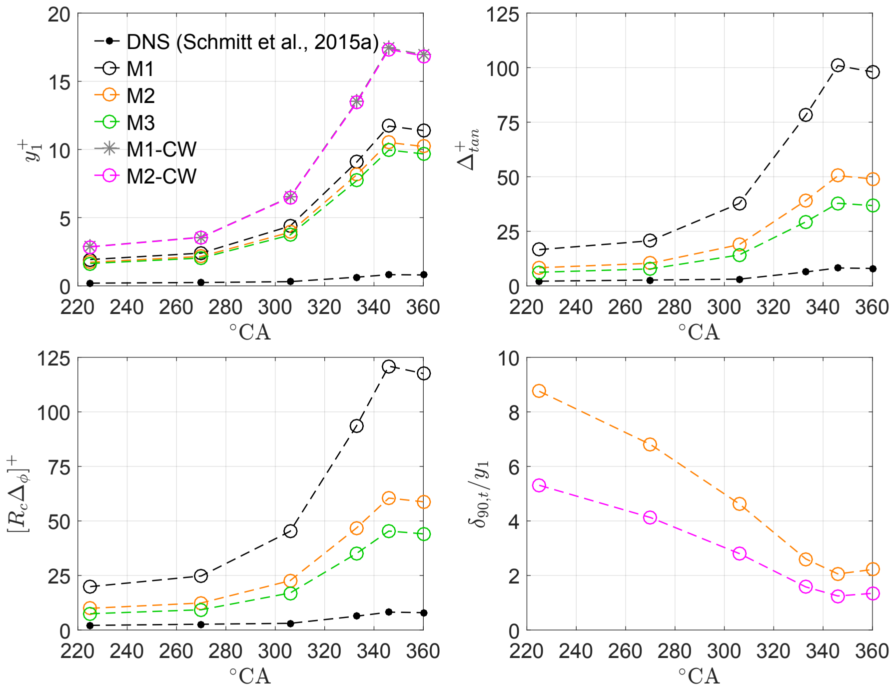


Figure 3: Variation of near-wall grid metrics throughout the compression stroke. Dimensionless wall-normal spacing (top left), tangential spacing (at the centre of the cylinder head; top right), azimuthal spacing at the cylinder liner (bottom left), and scaled thermal boundary layer thickness (bottom right). Scaling has been carried out according to cylinder head-averaged shear velocity and thermal boundary layer thickness observations in the reference DNS.

## 3. Results

The initial conditions for stages II and III are generated from stage I based on the HLR-WT model. Next, we show that the data in stage I is generated consistently with the model. For brevity, in Secs. 3.1-3.3 we only show results for HLR-WT, while model-to-model comparison is carried out for the compression stroke starting from Sec. 3.4.

### *3.1. Stage I (HLR-WT)*

Fig. 4 displays instantaneous velocity and modelled viscosity fields, elucidating the characteristics of the cyclic process during intake. Coherent flow features such as jet orientation (**a**), toroidal vortex ring location and intensity (**b**) as well as the advance of wall jets (**c**) are seen to vary between cycles. Concurrently, modelled viscosity frames, split into two halves, show the local influence of turbulence modelling. The left-hand side shows the modelled viscosity ($\nu_{mod}$) whereas the right-hand side displays the additive influence of the near-wall hybrid model ($\nu_{mod} - \nu_{sgs}$). Unlike the velocity field images, the two viscosity image halves are mirrored for a clearer comparison: both sides display fields corresponding to the left-

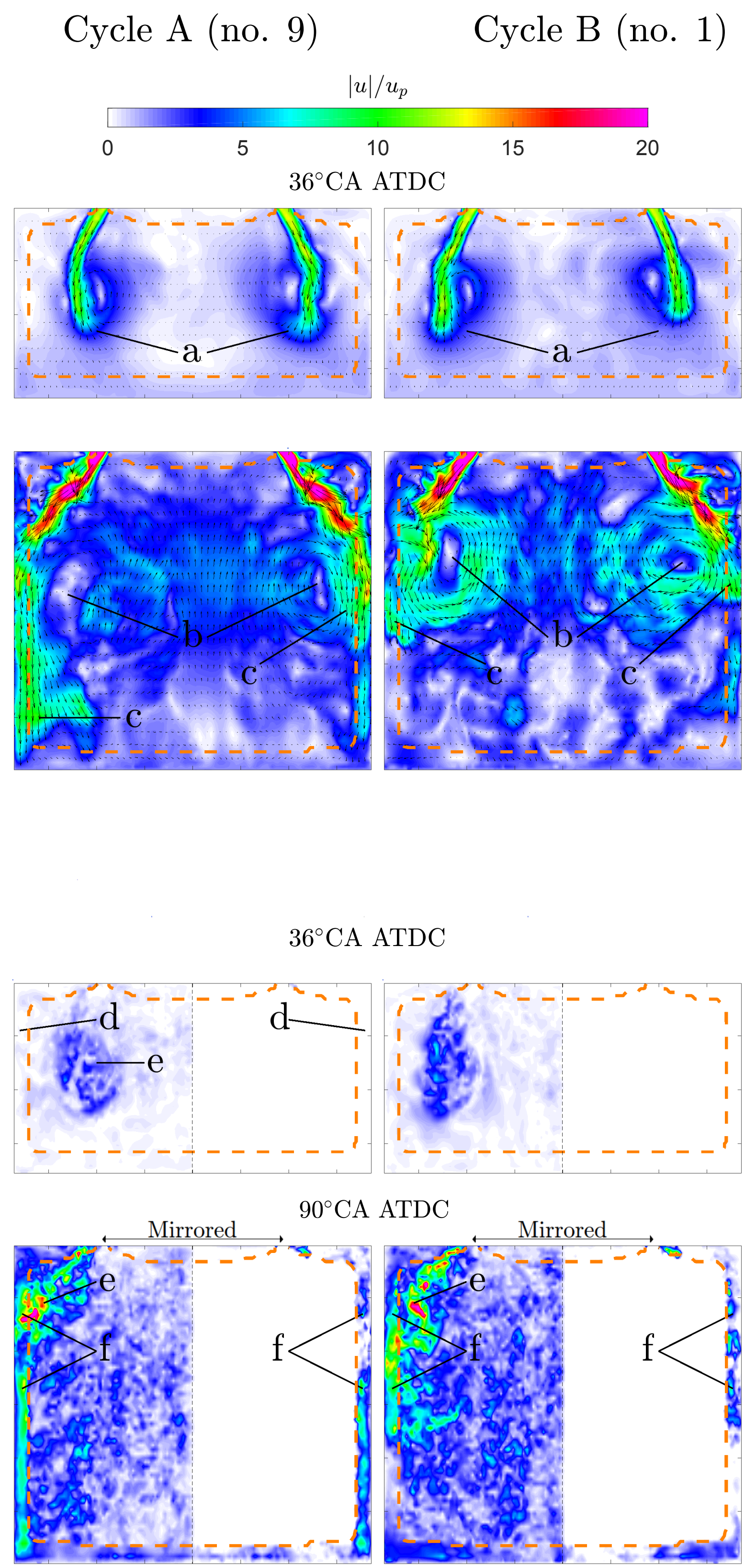


Figure 4: Stage I: velocity magnitude (top, scaled with mean piston velocity $u_p$) and modelled viscosity (bottom, scaled with molecular viscosity) snapshots on cycle A and cycle B along the same $r - z$ sampling plane. The orange dashed line denotes the LES/RANS interface position. Differences in dominant flow features including free jet orientation (a), vortex ring formation (b) and wall jet formation (c) are noted. On the LES side of the interface, modelled viscosity is entirely due to the SGS model (e). The zonal hybrid model is largely inactive during low Re conditions (d), activating with changing near-wall flow conditions (f).

hand side of the velocity fields. Due to the transient nature of the process, the flow Reynolds number and modelled contribution fluctuate considerably. During early intake (36°CA), $\nu_{mod}$ arises almost exclusively from the SGS model (**e**), while the hybrid model is suppressed due to low modelled production and interface SGS quantities (**d**). In such conditions, the wall model employs SGS quantities as input. Later (90°CA), higher modelled turbulence contribution can be noted at intake jets (**e**) and wall jets (**f**). (**e**) is again due to the SGS model while hybrid model activation is noted in the near-wall zones (**f**).

Fig. 5 illustrates phase and azimuth-averaged ($\langle \cdot \rangle$) mean axial velocities from the present HLR-WT simulation, compared with DNS (Schmitt et al., 2014b, $N = 57.8 \times 10^6$; spectral element code Nek5000) and LES (Keskinen et al., 2015, $N = 5.1 \times 10^6$; finite volume code OpenFOAM). Unlike the present work, cell layer removal and addition were not incorporated in the DNS and LES. The mean velocity profiles in Fig. 5 show a fair correspondence between all cases. While the HLR-WT shows a slight deviation in the initial jet orientation at 90°CA, the wall jet velocity profile is better described with the present computations compared to the reference LES. In general, deviations with the DNS result decrease when timing advances to 144° ATDC.

Axial velocity fluctuations (Fig. 6) also display good correspondence, although some overprediction is noted in near-wall values. When comparing fluctuation results it should be recalled that the reference LES result does not report a modelled fraction. The SGS model comparison of Buhl et al. (2017a) indicated that various models can provide a good agreement with experimental and DNS references. HLR-WT with the Smagorinsky model (not shown here) results in a relatively similar correspondence as the $\sigma$-model. Overall, the present mean and fluctuating velocity profiles provide a match to DNS which is at least equivalent to the reference LES which employs a different code and a finer grid.

### *3.2. Stage II (HLR-WT)*

Fig. 7 displays azimuthally averaged ($\langle \cdot \rangle_\phi$) temperature and velocity fields at the end of the intake stroke. The flow field is dominated by the toroidal vortex ring as a result of the incoming annular jet of fresh fuel-air mixture. In addition to the substantial local variations and asymmetry expected from scale-resolving simulations (not shown here), averaged quan-

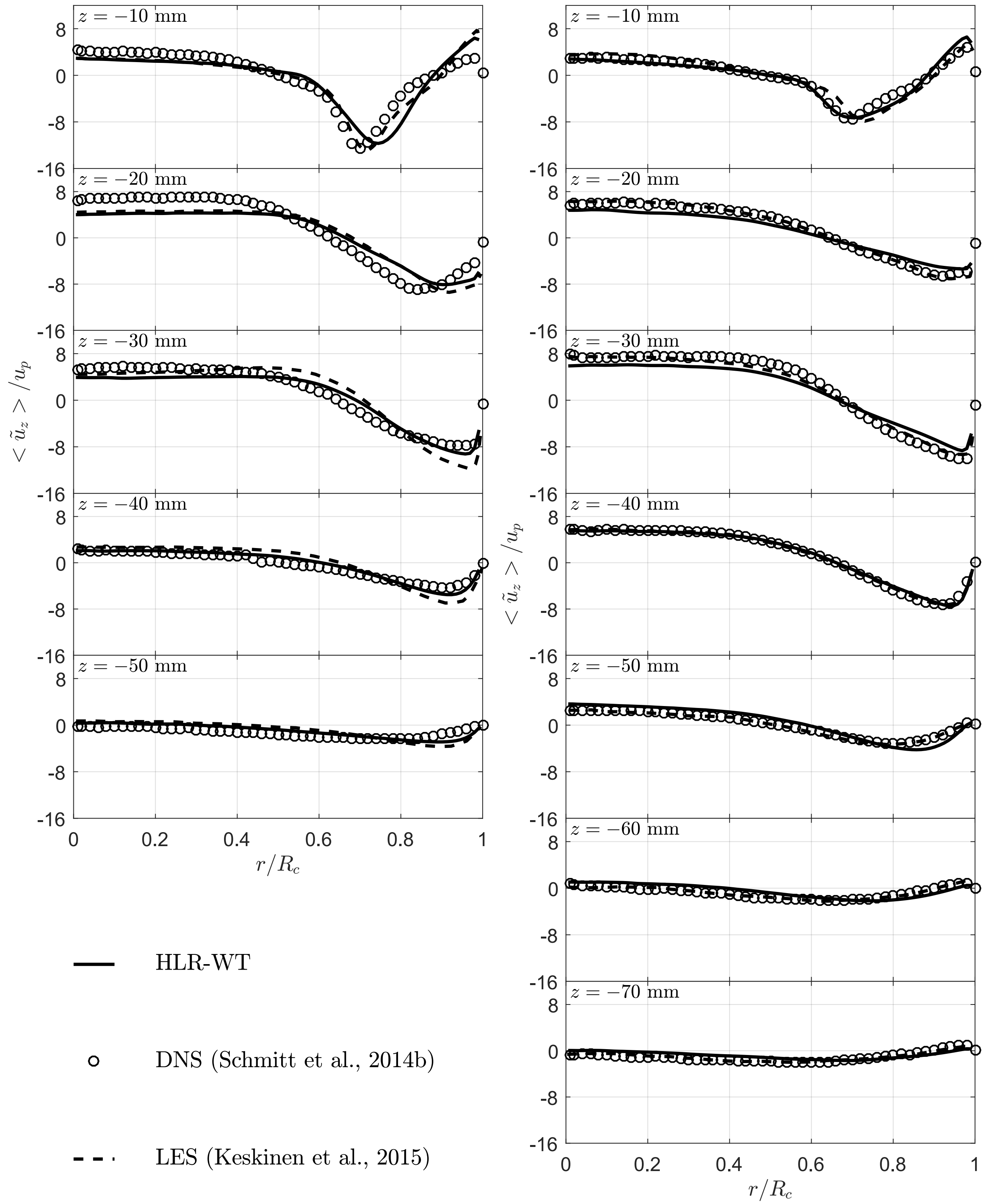


Figure 5: Stage I: axial mean velocities at observation planes, 90°CA ATDC (left) and 144°CA ATDC (right). Present results are averaged spatially in the azimuthal direction and phase-averaged over 17 consecutive cycles. Radial position $r$ is scaled with the cylinder radius $R_c$.

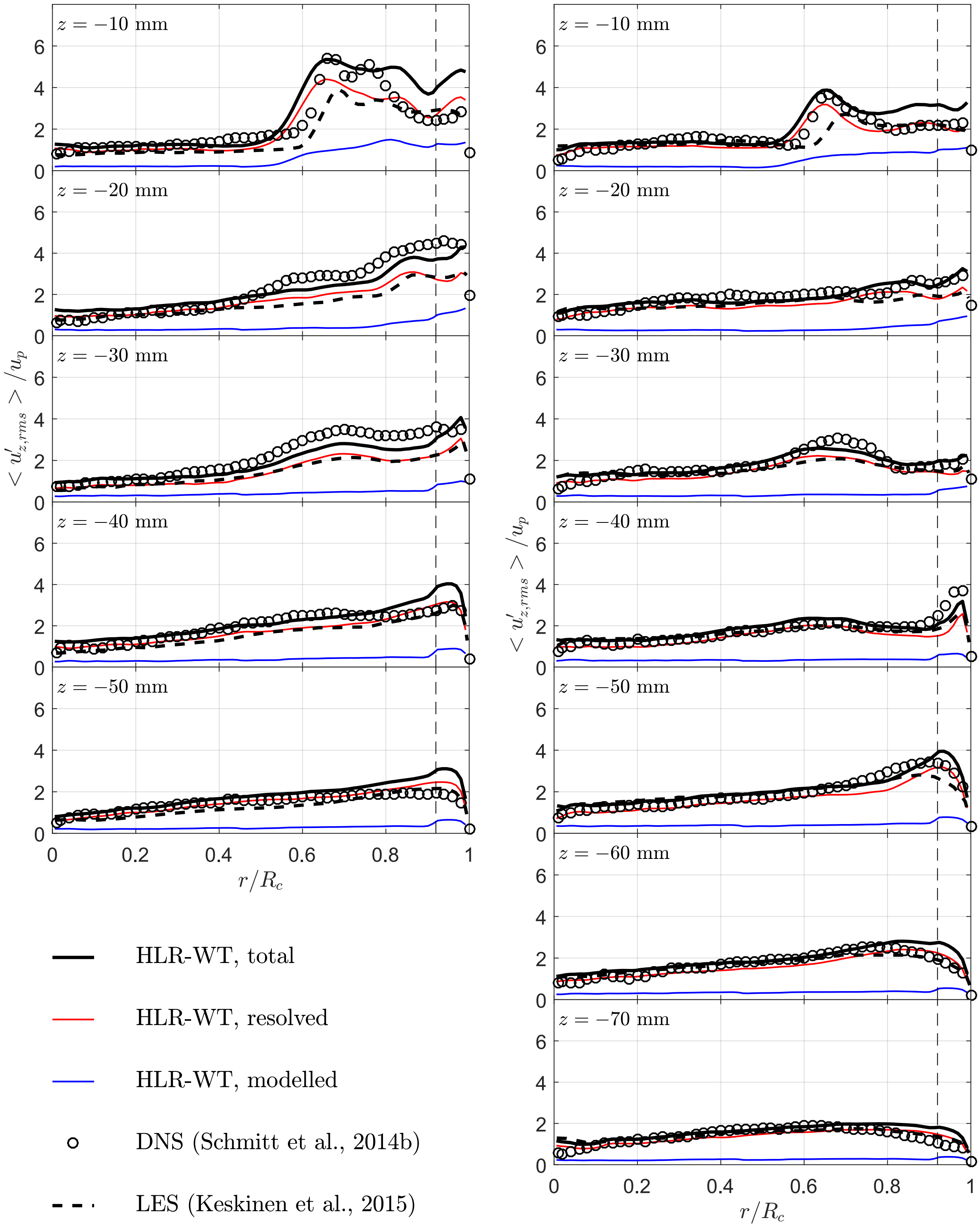


Figure 6: Stage I: axial rms velocity fluctuations at observation planes, 90°CA ATDC (left) and 144°CA ATDC (right). For the present HLR-WT cases, both resolved and modelled fractions are shown, while the vertical dashed lines denote the LES/RANS interface. Present results are averaged spatially in the azimuthal direction and phase-averaged over 17 consecutive cycles.

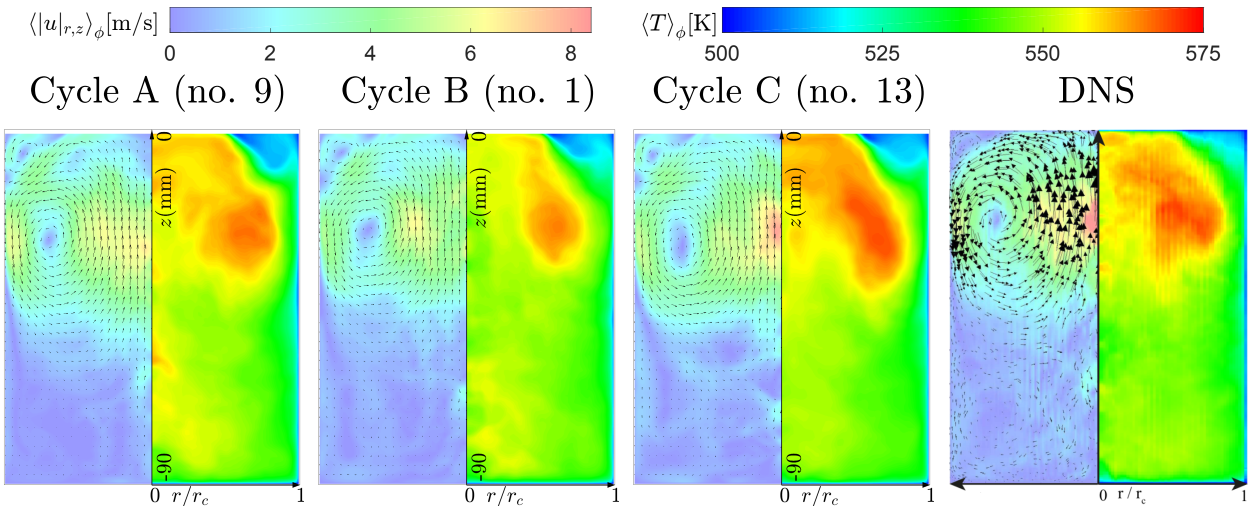


Figure 7: Stage II with different initialisation cycles (A, B, C): azimuthally averaged $r - z$-velocity fields (left half-frames) and azimuthally averaged temperature fields (right half-frames) at BDC. HLR-WT (three leftmost frames) and the reference DNS (Schmitt et al., 2015a, right).

tity fields vary depending on the initial fields imported from stage I computations. Foremost differences are observed in vortex ring and thermal field positioning. Despite slight variation between each cycle (A, B, C) and the reference DNS, the nominal cycle (A) BDC conditions appear to pose a sensible starting point for stage III.

### 3.3. *Stage III overview (HLR-WT)*

For brevity, an overview of simulation characteristics is shown here only for the HLR-WT model, whereas Secs. 3.4-3.7 concentrate on model-to-model assessment. Qualitatively similar results are however obtained also for the other approaches. The temperature and fuel mass fraction fields in Fig. 8 visualise how mixture formation progresses during the compression stroke. Close to BDC at 225°CA, temperature variation is $\mathcal{O}(100\text{ K})$ while the fuel-air mixture is still relatively inhomogeneous. Corresponding with initial unburned/burned conditions of stage II, thermal and fuel mass fraction fluctuations are negatively correlated. Conversely, at TDC, fuel and air are relatively well-mixed ($\overline{Y(H_2)}'_{rms,V}/\overline{Y(H_2)}_V = \mathcal{O}(10^{-3})$, where $\overline{\cdot}_V$ denotes volume-averaging) whereas differences have increased in the thermal field ($\overline{T}'_{rms,V}/\overline{T}_V = \mathcal{O}(10^{-1})$) due to concurrent compression and wall heat transfer.

While the LES/RANS interface in Fig. 8 places a considerable portion of the charge in the RANS zone, only minor and very localised influence thereof (where $\nu_{mod} > \nu_{sgs}$) is observed. Hence, the stage III HLR-WT computations are close to the WMLES simulations

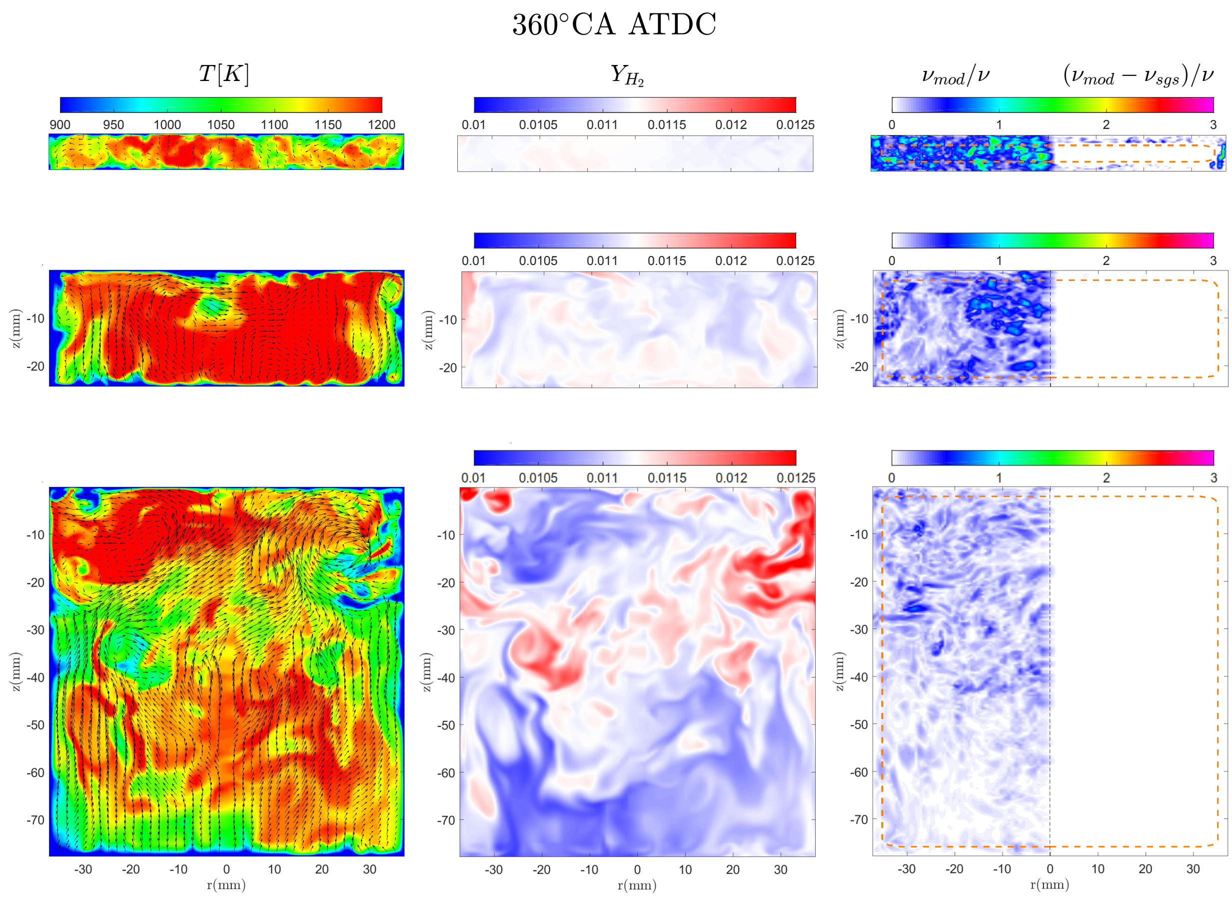


Figure 8: Stage III: instantaneous temperature (left, overlaid with $r-z$ velocity vectors), $H_2$ mass fraction (centre) and modelled viscosity (right) field snapshots throughout the compression stroke with HLR-WT (M3). The modelled viscosity snapshots show the LES/RANS interface (denoted by orange dashed lines) and are divided into halves showing $\nu_{mod}$ and $(\nu_{mod}-\nu_{sgs})$.

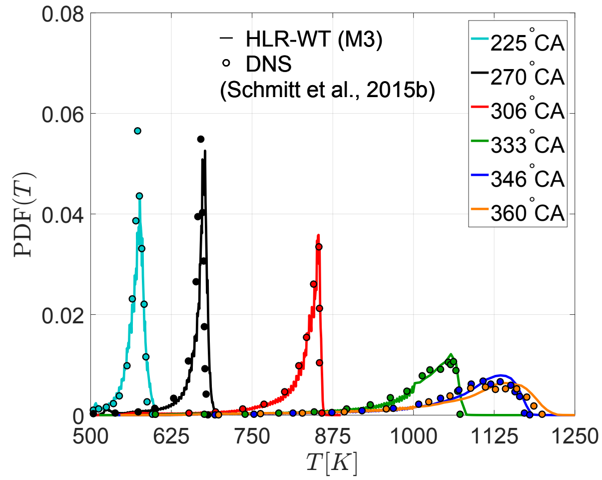


Figure 9: Stage III: Temperature PDFs at different time instances with the HLR-WT method (M3 grid) compared with the DNS reference (Schmitt et al., 2015b).

in terms of modelled contribution. Large thermal near-wall fluctuations convecting into the core charge are noted, corresponding with observations in the DNS (Schmitt et al., 2016a) and experimental investigations (Kaiser et al., 2013). Fig. 9 shows temperature probability density functions (PDFs) of the charge at different time instances. The influence of wall heat transfer towards TDC is evidenced by increasingly broader and shallower distributions.

### *3.4. Volume-averaged metrics*

Table 3 reports volume-averaged results at the middle of the compression stroke (270°CA) and at TDC (360°CA) for all the studied approaches and grids. The most significant approach-specific differences arise in the TDC thermal metrics, visualised in Fig. 10. WMLES-1-based computations result in the highest mean temperature deviations, and thermal fluctuation levels are considerably lower than in the WMLES-2 and HLR-WT cases. Increased resolution generally appears to improve results. In Table 3, the total fluctuation energy $\overline{k}_V$ and mean flow kinetic energy $\overline{KE}_V$ are defined as

$$\overline{k}_V = 0.5\overline{\left[(\tilde{u}_r - \langle\tilde{u}_r\rangle_\phi)^2 + (\tilde{u}_\phi - \langle\tilde{u}_\phi\rangle_\phi)^2 + (\tilde{u}_z - \langle\tilde{u}_z\rangle_\phi)^2\right]}_V + \overline{k_{mod}}_V \tag{17}$$

$$\overline{KE}_V = 0.5\overline{\left(\langle\tilde{u}_r\rangle_\phi^2 + \langle\tilde{u}_\phi\rangle_\phi^2 + \langle\tilde{u}_z\rangle_\phi^2\right)}_V \tag{18}$$

where $k_{mod}$ refers to either $k_{RANS}$ or $k_{sgs}$. A relative decline of turbulent fluctuations is noted when approaching TDC, in correspondence with the study of Mandanis et al. (2017). A late

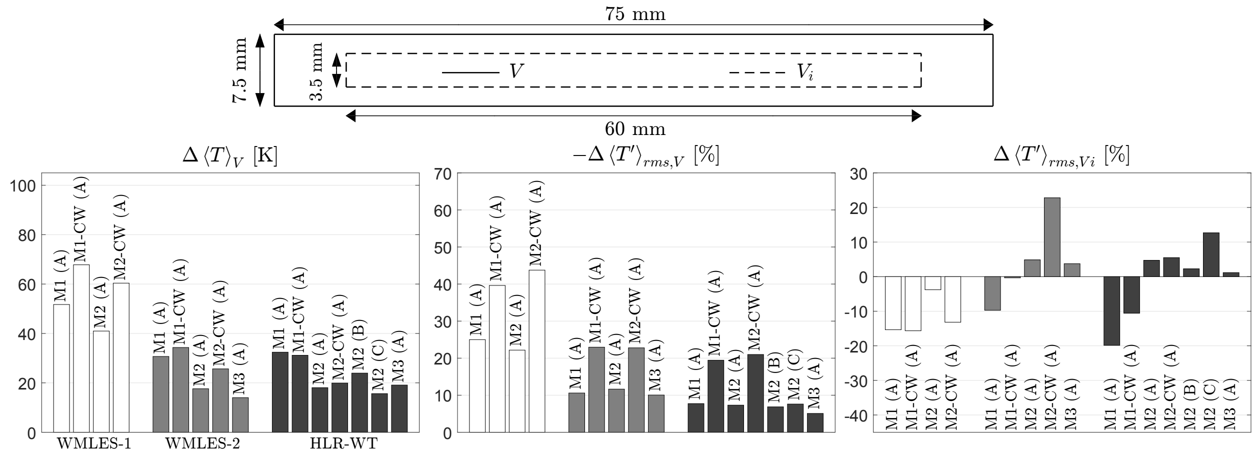


Figure 10: Stage III: visualisation of thermal metric differences between wall modelling approaches and DNS at TDC according to methodology, grid and cycle. Top: schematic of the cylinder geometry at TDC, showing the volume ($V$) and the inner volume ($V_i$). Volume-averaged mean temperature (left), volume-averaged temperature rms fluctuation (centre), inner volume-averaged temperature rms fluctuation (right).

compression decrease in fluctuating content with respect to experiments (Borée et al., 2002) was also noted by Toledo et al. (2007) in a simplified model engine. In the present low-order framework with non-uniform grids, numerical dissipation should be expected to have some effect as observed by Le Ribault et al. (2006) in the compression of a Taylor vortex. Noting the comparable sensitivity between (i) the improved approaches (WMLES-2 & HLR-WT), (ii) grid resolution, and (iii) the different initialisation cycles (A, B, C) in the results of Fig. 10 and Table 3, it appears challenging to make a systematic statement on the differences between WMLES-2 and HLR-WT. However, the improvements on WMLES-1 in terms of volume-averaged temperature and thermal fluctuations represent a distinct outcome of the presented results.

To explain the differing results at TDC, Fig. 11 depicts the temporal evolution of total heat transfer rate through cylinder walls. Minor differences to actual engine processes should be expected herein due to the sinusoidal piston positioning. Up to mid-compression, where grid resolution requirements remain lenient (Fig. 3) and wall modelling has little impact, only minor variation is noted between the cases. Thereafter, heat transfer rates increase markedly and WMLES-1 in particular begins to deviate from the DNS reference, especially with the CW grids. Accuracy is considerably improved with the WMLES-2 and HLR-WT approaches, whose total heat transfer trends are very similar with the latter displaying slightly lower grid sensitivity. Again, initialisation cycle selection has a noticeable but relatively mild effect on

Table 3: Collated results from stage III computations at two instances (270, 360°CA) of the compression stroke. In contrast to volume averaging (subscript $V$), $Vi$ denotes an internal part of the cylinder, limited by a 30 mm radius as well as (1) 7.5 mm (piston top/cylinder head) wall vicinity (up to 270°CA), (2) 2 mm wall vicinity (after 270°CA). For thermal metrics at 360°CA, the five most ($^*$) and least ($^\dagger$) accurate correspondences to the DNS are highlighted.

| Approach | Grid | Cycle | 270°CA $\overline{T}_V$ [K] | 270°CA $\overline{T}'_{rms,V}$ [K] | 270°CA $\overline{T}'_{rms,V_i}$ [K] | 270°CA $\overline{k}_V$ [m$^2$/s$^2$] | 270°CA $\overline{KE}_V$ [m$^2$/s$^2$] | 360°CA $\overline{T}_V$ [K] | 360°CA $\overline{T}'_{rms,V}$ [K] | 360°CA $\overline{T}'_{rms,V_i}$ [K] | 360°CA $\overline{k}_V$ [m$^2$/s$^2$] | 360°CA $\overline{KE}_V$ [m$^2$/s$^2$] |
|---|---|---|---|---|---|---|---|---|---|---|---|---|
| *DNS* | | | *659* | *29.7* | *6.8* | *2.50* | *1.30* | *1053* | *119.9* | *47.3* | *0.98* | *0.11* |
| WMLES-1 | M1 | A | 661 | 29.1 | 6.0 | 1.84 | 1.23 | 1105$^\dagger$ | 89.9$^\dagger$ | 40.0$^\dagger$ | 0.57 | 0.04 |
| WMLES-1 | M1-CW | A | 661 | 28.2 | 6.4 | 1.87 | 1.21 | 1121$^\dagger$ | 72.4$^\dagger$ | 39.9$^\dagger$ | 0.55 | 0.04 |
| WMLES-1 | M2 | A | 660 | 29.1 | 6.1 | 1.89 | 1.25 | 1094$^\dagger$ | 93.3 | 45.5$^*$ | 0.54 | 0.08 |
| WMLES-1 | M2-CW | A | 660 | 27.9 | 6.4 | 1.90 | 1.25 | 1113$^\dagger$ | 67.4$^\dagger$ | 41.1$^\dagger$ | 0.63 | 0.07 |
| WMLES-2 | M1 | A | 661 | 29.2 | 6.0 | 1.84 | 1.23 | 1084 | 107.2 | 42.7 | 0.58 | 0.04 |
| WMLES-2 | M1-CW | A | 661 | 28.5 | 6.4 | 1.88 | 1.21 | 1087$^\dagger$ | 92.4$^\dagger$ | 47.1$^*$ | 0.57 | 0.04 |
| WMLES-2 | M2 | A | 660 | 29.2 | 6.1 | 1.88 | 1.25 | 1071$^*$ | 105.9 | 49.6 | 0.55 | 0.07 |
| WMLES-2 | M2-CW | A | 660 | 28.2 | 6.1 | 1.90 | 1.25 | 1079 | 92.6$^\dagger$ | 58.1 | 0.59 | 0.06 |
| WMLES-2 | M3 | A | 660 | 29.7 | 7.1 | 1.95 | 1.24 | 1067$^*$ | 107.8 | 49.1$^*$ | 0.59 | 0.04 |
| HLR-WT | M1 | A | 661 | 29.3 | 6.0 | 1.85 | 1.23 | 1086 | 110.6$^*$ | 37.9$^\dagger$ | 0.55 | 0.04 |
| HLR-WT | M1-CW | A | 661 | 29.0 | 6.1 | 1.86 | 1.21 | 1084 | 96.6 | 42.3 | 0.52 | 0.06 |
| HLR-WT | M2 | A | 660 | 29.4 | 6.2 | 1.89 | 1.26 | 1071$^*$ | 111.1$^*$ | 49.5 | 0.52 | 0.08 |
| HLR-WT | M2-CW | A | 660 | 28.8 | 6.3 | 1.90 | 1.25 | 1073 | 94.7 | 49.9 | 0.54 | 0.05 |
| HLR-WT | M2 | B | 659 | 29.3 | 6.0 | 1.61 | 1.24 | 1077 | 111.7$^*$ | 48.4$^*$ | 0.50 | 0.05 |
| HLR-WT | M2 | C | 660 | 29.2 | 6.4 | 1.33 | 1.53 | 1069$^*$ | 110.8$^*$ | 53.3$^\dagger$ | 0.55 | 0.10 |
| HLR-WT | M3 | A | 661 | 29.8 | 7.1 | 1.95 | 1.25 | 1072$^*$ | 113.8$^*$ | 47.9$^*$ | 0.56 | 0.06 |

the trends.

### *3.5. Near-wall profiles*

The wall-bounded flows in ICEs are highly non-standard in terms of their structure and the commonly utilised scaling laws. Hence, nondimensional velocity and temperature profiles provide an informative impression of wall model functionality. In Fig. 12, such profiles are plotted at 270°CA, 306°CA and 346°CA for the M1-CW and M2 grids. Velocity is scaled here as $|u|^+ = |u|/\overline{u_\tau}_{90}$, wall-normal distance as $z^+ = (z/\nu_w)\overline{u_\tau}_{90}$, and temperature as $T^+ = (T_w - T)\rho_w c_{p,w}\overline{u_\tau}_{90}/\overline{q_w}_{90}$. $\overline{\cdot}_{90}$ denotes instantaneous spatial averaging over 0-90 % of the cylinder radius in analogy with the DNS.

Several contrasting properties can be highlighted between the models. Both WMLES-1 and WMLES-2 yield velocity scaling closer to the Werner-Wengle power law (Eq. 11) and the linear-log law than to the DNS results (**a**). Hence, excessive $|u|^+$ values (representing underprediction of $u_\tau$) are observed towards TDC. The finer near-wall grid supplies better results as the near-wall grid point is located within the viscous sublayer for a longer time, which is an expected result based on the observations of Ma et al. (2017a). Scaled tem-

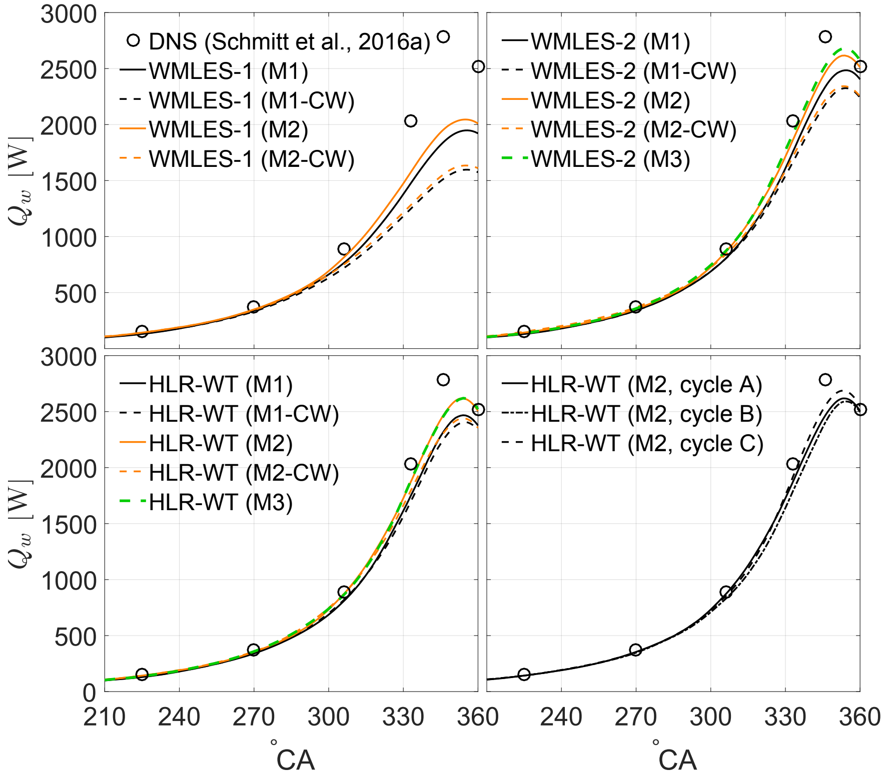


Figure 11: Stage III: total wall heat transfer rate throughout the compression stroke with WMLES-1 (top left), WMLES-2 (top right) and HLR-WT (bottom left) approaches and different grids with cycle A. The influence of initialisation cycle selection is shown with HLR-WT and the M2 grid (bottom right).

perature profiles however differ conspicuously between WMLES-1 and WMLES-2, with the former erroneously following a linear-logarithmic trend (**b**), consistent with its formulation. Remarkably, WMLES-2 results in relatively accurate thermal scaling despite the inclusion of the mismatched $u_\tau$ as an input to the heat transfer model.

In contrast to the two algebraic models, HLR-WT scaling appears relatively accurate and consistent between velocity and thermal boundary layers, indicating that fairly appropriate predictions are obtained for both wall shear stress and wall heat flux over the highly dynamic compression stroke. Furthermore, this mean profile result is replicated with different grids in terms of both near-wall and core flow resolution. Such results could potentially be expected from 1-D non-equilibrium models: Ma et al. (2017b) reported favourable results for both momentum and thermal boundary layers in their measurement-based near-wall model comparison. In comparison to their work (Ma et al., 2017a,b), the present non-equilibrium model is conceptually simpler as individual imbalance contributions are not considered.

Fig. 13 displays near-wall profiles for temperature fluctuations and total (resolved +

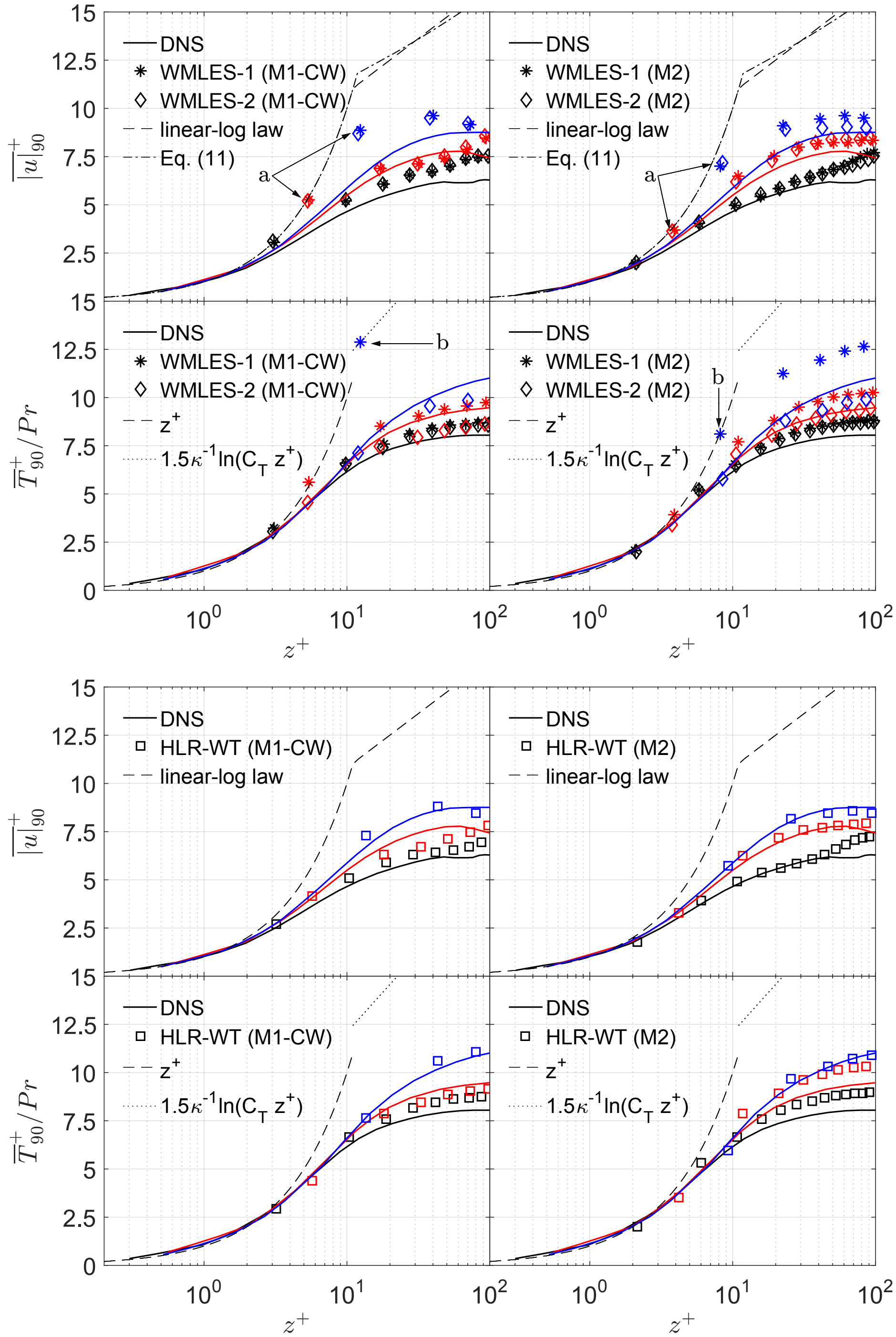


Figure 12: Stage III: scaled near-wall mean profiles of velocity magnitude (top frames) and temperature (bottom frames) at 270°CA (black), 306°CA (red) and 346°CA (blue). WMLES-methods (top) and HLR-WT (bottom) with coarse (M1-CW, left) and intermediate (M2, right) grids. Variables are scaled as $z^+ = (z/\nu_w)\overline{u_\tau}_{90}$, $|u|^+ = |u|/\overline{u_\tau}_{90}$, $T^+ = (T_w - T)\rho_w c_{p,w}\overline{u_\tau}_{90}/\overline{q_w}_{90}$.

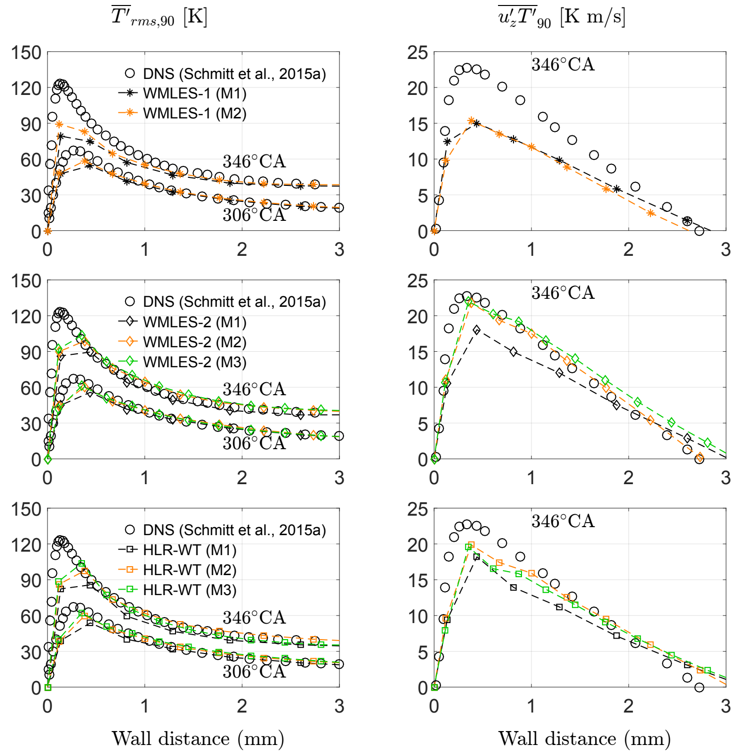


Figure 13: Stage III, cycle A: cylinder head near-wall profiles of rms temperature fluctuations (centre) and total (resolved + modelled) turbulent heat flux (right). WMLES-1 (top), WMLES-2 (centre) and HLR-WT (bottom) approaches.

modelled) turbulent heat flux. While differences in $\overline{T}'_{rms}$ are minute at 306°CA, the later timing of 346°CA shows greater result variation. Core grid refinement improves both $\overline{T}'_{rms}$ and turbulent heat flux profiles – however, the high near-wall $\overline{T}'_{rms}$ peak in the DNS is not accurately captured with any of the present computations. In comparison to WMLES-1, WMLES-2 and HLR-WT cases yield improved fluctuation profiles. In correspondence with the results in Table 3, CW grid results (not shown here for brevity) produce a more substantial underprediction of the fluctuations.

### *3.6. Local metrics and the wall heat transfer mechanism*

Fig. 14 illustrates instantaneous wall heat flux distributions on the cylinder head ($z = 0$) surface at 306°CA and 360°CA. In addition, PDFs for the heat transfer coefficient $\alpha = q_w/(\overline{T}_V - T_W)$ are shown for the TDC time instance. As noted by Schmitt et al. (2016b), the prevalent local regions of high heat flux are primarily due to wall-impinging hot streams. The turbulent scales reduce substantially during compression due to the dramatic decrease in kinematic viscosity, particularly close to the (relatively cold) wall. At 306°CA, the different models yield relatively similar distributions that coincide qualitatively with the DNS, although a clear difference in the resolved scales is already visible. Such a result similarity corresponds to the near-wall profiles in Figs. 12 and 13 – indeed, at 306°CA the wall-adjacent M2 grid node is still within the viscous sublayer ($y_1^+ \approx 4$).

TDC conditions, resulting in minuscule scales and vast local variations in the DNS fields, offer considerably different results. While near-wall scales have evidently reduced in the wall-modelled computations, the smallest structures found in the DNS are far beyond the reach of the present grids. Hence, comparison is additionally carried out with DNS data box-filtered onto the M2 surface grid (FDNS), representing a more feasible point of reference for the wall-modelled methods (Yang et al., 2017). Such filtering effectively results in a slightly narrower heat transfer coefficient PDF. While the present wall-modelled heat transfer distributions expectedly correspond better with the FDNS than with the DNS, result differences are not entirely mitigated for any of the present computations. With the M2 grid, WMLES-1 shows the smallest local variations, as evidenced also by the narrow, high-peak shape of the corresponding PDF. Comparing WMLES-2 and HLR-WT (with approximately similar mean values), the latter displays finer structures with higher local maxima and slightly improved $\alpha$ correspondence against the DNS. Such differences indicate that there are differences as to how the peaks are formed (to be discussed later).

With the M2-CW grid, the differences between M2 observations appear to have increased further. While mean values remain relatively similar with WMLES-2 and HLR-WT, the replication of local heat transfer variation has clearly deteriorated. For rationale thereto, we can refer to the wall-normal spacing relative to the boundary layer thickness $\delta_{90}$ (Fig. 3). Close to TDC, the CW spacing gradually approaches $\delta_{90}$, posing a suboptimal situation from the perspective of wall modelling: Larsson et al. (2016) state an optimal wall-modelled layer to be ca. 20% of the boundary layer thickness. It is not immediately apparent how such criteria should be formed for the characteristically specific in-cylinder flows. It should however be noted that wall-modelled scale-resolving simulations are not generally known for high-quality wall flux fluctuation predictions (Yang et al., 2017).

As the local heat flux distributions in Fig. 14 cannot indicate wall-normal convection,

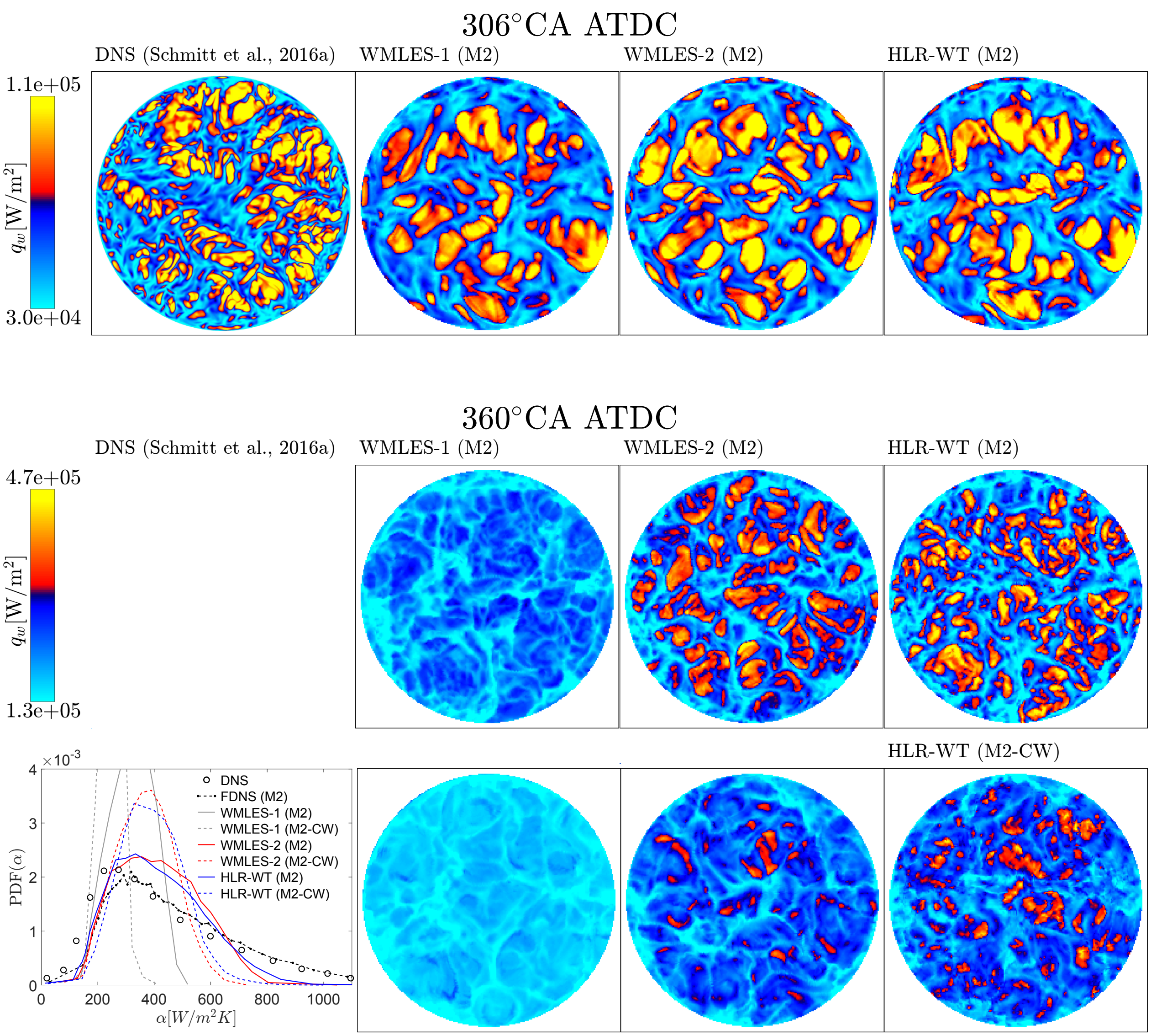


Figure 14: Stage III, cycle A: instantaneous cylinder head heat transfer rate depicted at 306°CA (top) and at TDC (bottom). For TDC, distributions are shown with both M2 and M2-CW grids. Due to the high difference in resolved scales between the DNS and the present simulations at TDC, a filtered DNS distribution (FDNS [M2]) is additionally displayed. Alongside the images, heat transfer coefficient PDFs over all cylinder walls are illustrated.

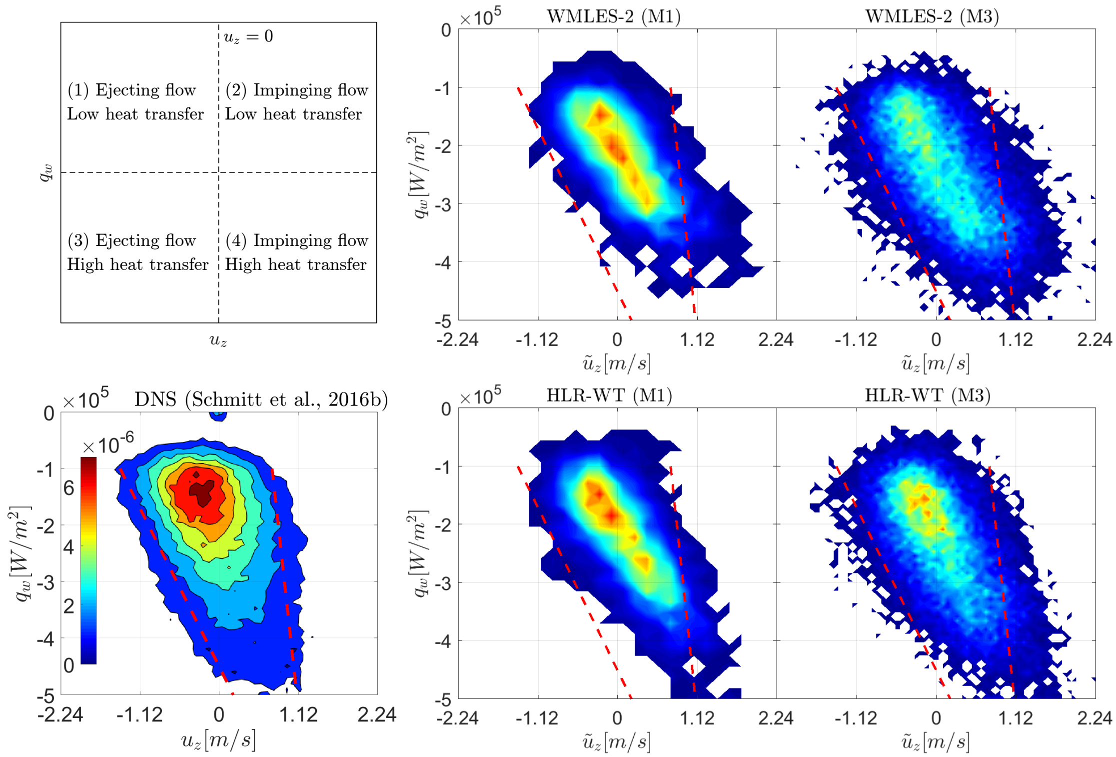


Figure 15: Stage III, cycle A: joint PDFs of wall-normal velocity at $z = -0.9375$ mm and wall heat flux at the corresponding wall location at 346°CA. The reference DNS (bottom left) is shown alongside WMLES-2 (top right) and HLR-WT (bottom right) computations with differing core grid resolutions. Red dashed guide lines (adopted from the DNS trends) are identical in each frame.

instrumental to the wall heat transfer mechanism of impinging ($u_z > 0$) and ejecting ($u_z < 0$) streams (Schmitt et al., 2016b), additional insight is sought by correlating the wall heat flux with the adjacent flow field. Fig. 15 presents joint PDFs of $u_z$ and $q_w$ for WMLES-2 and HLR-WT across the cylinder head surface and illustrates conceptual interpretations of different PDF regions. The diagonally oriented distributions signify the high contribution of flow types 1 (ejecting with low heat transfer) and 4 (impinging with high heat transfer). Hence, the heat transfer mechanism observed in the DNS appears to be qualitatively replicated. In comparison to the DNS, type 4 flows are slightly overrepresented, and the distributions are more tilted. With HLR-WT, both grids suggests a minor improvement over the corresponding WMLES-2 case.

### 3.7. Model functionality in different flow zones

In order to more closely inspect the minute differences in local near-wall metrics observed between WMLES-2 and HLR-WT, model functionality is examined in different local flow regions. The present wall-modelled simulations cannot evidently be expected to accurately reproduce the small-scale flow physics in the near-wall region. However, a filtered DNS distribution may be used to illustrate how heat transfer models should respond to ejecting and impinging flows on a larger scale.

Fig. 16 displays the scaled heat flux $q_w/\overline{q_w}_{90}$ and is overlaid with the wall shear stress field. With both WMLES-2 and HLR-WT, ejection locations can be identified by near-wall counterflow with low local heat transfer, consistent with expectations from the FDNS. For impinging flow, heat flux maxima should be expected at stagnation regions. With WMLES-2, such local maxima are largely absent: instead, highest heat transfer values are generally located where the flow is tangential. Indeed, this property, resulting from the strong dependence between $q_w$ and $u_\tau$ (Eq. 14), was acknowledged by Plensgaard (2013). An improved representation of stagnation regions is noted with HLR-WT, where the link between $\tau_w$ and $q_w$ is considerably weaker than in the algebraic models. The plots in Fig. 16 demonstrate how the local differences occur by applying WMLES-2 instantaneously on the HLR-WT field in wall-adjacent locations A, B and C. Approximately similar predictions are noted in ejecting (A) and tangential (B) locations (where a correlation between $\tau_w$ and $q_w$ is expected) while a large difference is noted in the impinging flow (C). Here, the combination of a low $u_\tau$ value and high temperature difference results in only a moderate heat flux with WMLES-2. In contrast, the HLR-WT profile is considerably influenced by the imbalance term $I_h = (q_h - q_w)/\Delta y$ within the solution of Eq. (16), increasing the near-wall gradient. Effectively, the utilisation of two near-wall main grid points in the model of Nuutinen et al. (2014) permits the incorporation of an additional piece of information on the local flow state.

### *3.8. Influence of the HLR-WT non-equilibrium model*

As detailed in Sec. 2.4.2, the HLR-WT wall treatment solves simplified 1-D TBLEs with a non-equilibrium model that incorporates values of variables at both first and second wall-adjacent cell centres. To specifically illustrate how the non-equilibrium model influences results, we modify the HLR-WT approach so that imbalance terms are cancelled within the iterative routine, i.e. $I_m = I_h = 0$ in Eqs. (15) and (16). This reduces the approach to a 1-D equilibrium model (HLR-WT-EQ) and omits the influence of the second near-wall grid

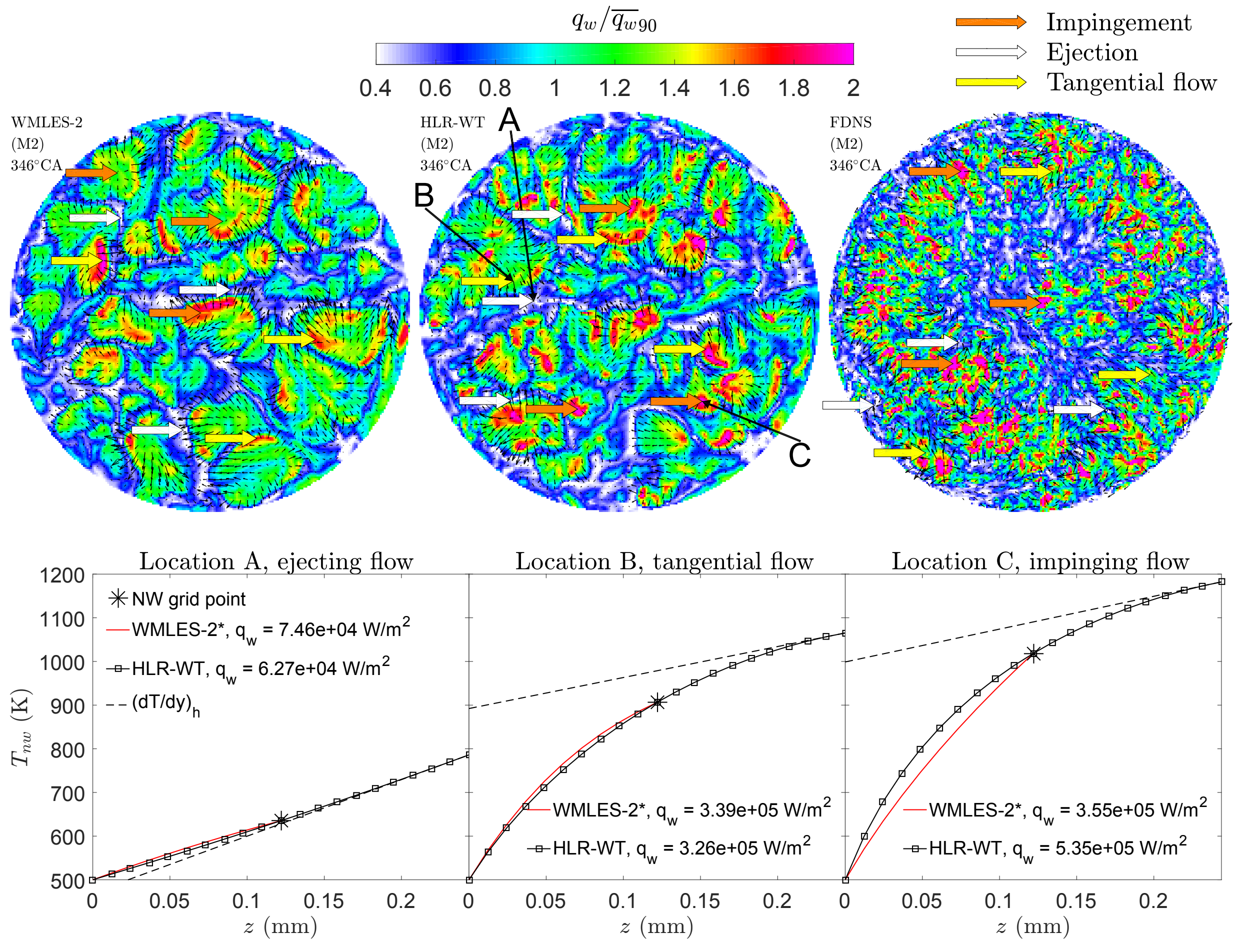


Figure 16: Stage III, cycle A. Top: normalised instantaneous cylinder head heat flux distribution $q_w/\overline{q_w}_{90}$ overlaid with wall shear stress vectors at 346°CA with WMLES-2 (left) and HLR-WT (centre) approaches. Filtered DNS fields are shown as a reference (right). Arrows exemplify locations of impingement (orange), ejection (white) and tangential flow (yellow). Bottom: illustration of instantaneous wall model predictions throughout the near-wall cell in different flow types. In addition to the HLR-WT subgrid solution and the algebraic WMLES-2 profile, dashed lines denote the temperature gradient determined by $q_h$, which functions as a boundary condition in HLR-WT. The superscript (*) denotes that the WMLES-2 wall model is instantaneously applied on the HLR-WT field.

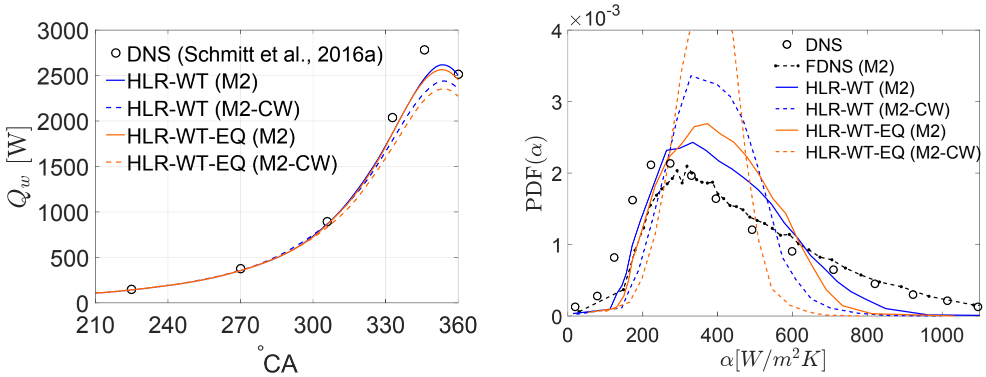


Figure 17: Stage III, cycle A. Heat transfer comparison between HLR-WT and its equilibrium modification (HLR-WT-EQ). Total wall heat transfer rate throughout compression (left) and wall heat transfer coefficient PDF at TDC (right).

point. Fig. 17 displays the resulting effects in terms of total wall heat transfer and heat flux fluctuations with the M2 and M2-CW grids. In terms of total heat flux, the non-equilibrium model results in a mild improvement which is more pronounced in the case of the coarse near-wall grid. The wall heat transfer coefficient PDFs differ more clearly: use of the non-equilibrium model results in higher contributions of both low and high heat transfer extrema, in better correspondence with the DNS. These observations indicate that the non-equilibrium model yields clear result benefits in the HLR-WT approach.

### *3.9. Discussion*

With the present wall-modelled cases, computational cost scales relatively leniently when core grid resolution is increased: as both near-wall and core grid scales are not highly detached (Table 2), additional time step restrictions remain mild. This is in strong contrast to wall-resolved LES and even wall normal-resolved hybrid methods, where significant bottlenecks may arise. Unlike increases in cell count which can be managed with increased parallelisation in the case of highly scalable codes, temporal parallelisation cannot be similarly incorporated (Larsson and Wang, 2014). Hence, a large number of time steps considerably influences simulation turnaround time.

The simplicity and low computational cost of algebraic models is an attractive aspect in comparison to 1-D methods. The fair performance of WMLES-2 in the present work encourages further investigation of such models. The DNS revealed that semi-local scaling (employing local material properties) results in increased similarity between the nondimensional boundary layer profiles (Schmitt et al., 2015a), offering one possible development pathway. Novel compressible flow formulations analogous to the Van Driest transformation (e.g. Trettel and Larsson, 2016) can also be incorporated. Still, the most challenging hurdle for algebraic models may be induced by the fundamental complexity of ICE boundary layers, highlighted in other contemporary modelling-related studies (Ma et al., 2017a; Renaud et al., 2018).

It needs to be noted that ICE flows entail a much broader scope than what the present, highly simplified configuration represents. In addition to the influence of engine speed, coherent charge motions such as swirl, tumble or squish flows are routinely present in real ICE configurations and are expected to influence the scaled profiles and the functionality of wall models. Indeed, further wall-modelled investigations of well-documented non-reacting engine configurations could provide valuable additional insight to complement the present work. Moreover, wall modelling for high Reynolds number reacting flows, outside of the scope of the present work, is a highly challenging and emerging research area. Thereby, the results of the present study certainly pose some limitations and their projection to the real engine context may not be completely straightforward.

## 4. Summary and conclusions

Wall-modelled scale-resolving simulations were carried out in engine-like flows using DNS data as a reference. The computations involved three consecutive stages, namely (I) a multi-cycle cold flow process, (II) fuel-air intake, and (III) charge compression. Stages I and II were first assessed with the HLR-WT model, yielding an acceptable match to the reference DNS. Stage III, the study focus, comprised assessment of two algebraic wall models (WMLES-1, WMLES-2) and a 1-D subgrid-based approach (HLR-WT). Grids differing in both off-wall and near-wall resolution were investigated.

In the compression stroke it was found that WMLES-1, utilising standard wall laws, led to a substantial and highly grid dependent underprediction of wall heat transfer and thermal fluctuations. WMLES-2 and HLR-WT, entailing wall models developed in the context of engine flows, delivered considerably improved predictions of volume-averaged thermal metrics with lower grid sensitivity.

Scaled near-wall profiles indicated that all approaches yielded acceptable results when the near-wall grid point was within the viscous sublayer. Outside of the sublayer, wall shear stress was underpredicted with the algebraic models due to their relatively close adherence with the Werner-Wengle power law. WMLES-1 continued a similar trend with thermal scaling, explaining the near-wall grid sensitivity in thermal predictions. In contrast, the engine-targeted WMLES-2 (based on the model of Han and Reitz (1997)) provided considerably improved thermal scaling. For all grids tested in this work, HLR-WT resulted in fairly appropriate scaling throughout the compression stroke for both momentum and thermal boundary layers.

With WMLES-2 and HLR-WT, closer inspection of near-wall processes indicated a qualitative replication of the near-wall impingement-ejection process observed in the DNS. The present grids and methods were however not able to fully capture the wall heat transfer fluctuations. In the present configuration, HLR-WT provided a slight enhancement in the reproduction of such fluctuations and an improved description of heat transfer maxima associated with impinging streams. Comparison with an equilibrium modification of HLR-WT indicated that the non-equilibrium model improved heat transfer predictions.

Core grid refinement generally improved the fidelity of near-wall fluctuating metrics and the impingement-ejection process. In contrast, use of coarse near-wall grids in the wall-normal direction resulted in a substantial deterioration of such fidelity with all models. The results provide evidence of the potential of the HLR-WT and WMLES-2 approaches for the prediction of near-wall ICE processes. While further charge formation patterns and engine conditions with differing near-wall profiles should be tested for a more comprehensive understanding, the reported observations augment the recent notions (Ma et al., 2017a,b) that advanced near-wall models may offer benefits for in-cylinder flow and heat transfer simulations.

## Acknowledgements

The authors gratefully acknowledge funding from the TEKES (the Finnish Funding Agency for Innovation) project "FLEX$^E$" and computational resources provided by the Aalto

Science-IT project. Funding from the Swiss Federal Office of Energy (grant no. SI/501584-01) and the Swiss Competence Centre for Energy and Mobility (CCEM project "RENERG2") is also gratefully acknowledged. The first author acknowledges support from the Finnish Foundation for Technology Promotion Gasum Gas Fund. The authors thank George Giannakopoulos and Christos Frouzakis for their assistance in DNS data acquisition and processing. The authors also acknowledge the International Energy Agency Combustion Technology Collaboration Program on Clean and Efficient Combustion for promoting the collaboration that made this work possible.

## References

Angelberger, C., Poinsot, T., Delhay, B., 1997. Improving near-wall combustion and wall heat transfer modeling in SI engine computations. SAE Technical Paper 972881.

Borée, J., Maurel, S., Bazile, R., 2002. Disruption of a compressed vortex. Phys. Fluids 14 (7), 2543–2556.

Buhl, S., Dietzsch, F., Buhl, C., Hasse, C., 2017a. Comparative study of turbulence models for scale-resolving simulations of internal combustion engine flows. Comput. Fluids 156, 66–80.

Buhl, S., Gleiss, F., Köhler, M., Hartmann, F., Messig, D., Brücker, C., Hasse, C., 2017b. A combined numerical and experimental study of the 3D tumble structure and piston boundary layer development during the intake stroke of a gasoline engine. Flow Turbul. Combust. 98, 579–600.

CD-Adapco, 2013. Methodology, STAR-CD version 4.20.

Chaouat, B., 2017. The state of the art of hybrid RANS/LES modeling for the simulation of turbulent flows. Flow Turbul. Combust. 99, 279–327.

Choi, H., Moin, P., 2012. Grid-point requirements for large eddy simulation: Chapman's estimates revisited. Phys. Fluids 24 (011702).

Craft, T., Gerasimov, A., Iacovides, H., Launder, B., 2002. Progress in the generalization of wall-function treatments. Int. J. Heat Fluid Flow 23 (2), 148–160.

di Mare, F., Knappstein, R., Baumann, M., 2014. Application of LES-quality criteria to internal combustion engine flows. Comput. Fluids 89, 200–213.

Enaux, B., Granet, V., Vermorel, O., Lacour, C., Thobois, L., Duguè, V., Poinsot, T., 2011. Large eddy simulation of a motored single-cylinder piston engine: Numerical strategies and validation. Flow Turbul. Combust. 86, 153–177.

Frouzakis, C., Giannakopoulos, G., Wright, Y., Boulouchos, K., 2017. Direct numerical simulations for internal combustion premixed gas engines: First steps, challenges and prospects. Proceedings of the 13th International Congress on Engine Combustion Processes (ENCOM), Ludwigsburg, Germany, 16th/17th March 2017.

Han, Z., Reitz, R., 1997. A temperature wall function formulation for variable-density turbulent flows with application to engine convective heat transfer modeling. Int. J. Heat Mass Transfer 40 (3), 613–625.

Hasse, C., 2016. Scale-resolving simulations in engine combustion process design based on a systematic approach for model development. Int. J. Engine Res. 17 (1), 44–62.

Hattori, H., Nagano, Y., 2004. Direct numerical simulation of turbulent heat transfer in plane impinging jet. Int. J. Heat Fluid Flow 25 (5), 749–758.

Haworth, D., Jansen, K., 2000. Large-eddy simulation on unstructured deforming meshes: towards reciprocating IC engines. Comput. Fluids 29 (5), 493–524.

He, C., Leudesdorff, W., di Mare, F., Sadiki, A., Janicka, J., 2017. Analysis of in-cylinder flow field anisotropy in IC engine using large eddy simulation. Flow Turbul. Combust., 1–31.

Iwamoto, K., Suzuki, Y., Kasagi, N., 2002a. Database of fully developed channel flow, THTLAB internal report, no. ILR-0201. Tech. rep., THTLAB, Dept. of Mech. Eng., The Univ. of Tokyo.

Iwamoto, K., Suzuki, Y., Kasagi, N., 2002b. Reynolds number effect on wall turbulence: toward effective feedback control. Int. J. Heat Fluid Flow 23 (5), 678–689.

Jainski, C., Lu, L., Dreizler, A., Sick, V., 2013. High-speed micro particle image velocimetry studies of boundary-layer flows in a direct-injection engine. Int. J. Engine Res. 14 (3), 247–259.

Jakirlić, S., Kadavelil, G., Kornhaas, M., Schäfer, M., Sternel, D., Tropea, C., 2010. Numerical and physical aspects in LES and hybrid LES/RANS of turbulent flow separation in a 3-D diffuser. Int. J. Heat Fluid Flow 31 (5), 820–832.

Jakirlić, S., Kniesner, B., Kadavelil, G., 2011. On interface issues in LES/RANS coupling strategies: a method for turbulence forcing. J. Fluid Sci. Technol. 6 (1), 56–72.

Kaiser, S., Schild, M., Schulz, C., 2013. Thermal stratication in an internal combustion engine due to wall heat transfer measured by laser-induced fluorescence. Proc. Combust. Inst. 34, 2911–2919.

Kawai, S., Larsson, J., 2013. Dynamic non-equilibrium wall-modeling for large eddy simulation at high Reynolds numbers. Phys. Fluids 25 (1), 015105.

Keskinen, J.-P., Vuorinen, V., Kaario, O., Larmi, M., 2015. Large eddy simulation of a piston-cylinder assembly: The sensitivity of the in-cylinder flow field for residual intake and in-cylinder velocity structures. Comput. Fluids 122, 123–135.

Keskinen, K., Kaario, O., Nuutinen, M., Vuorinen, V., Koch, J., Wright, Y. M., Larmi, M., Boulouchos, K., 2017. Hybrid LES/RANS with wall treatment in tangential and impinging flow configurations. Int. J. Heat Fluid Flow 65, 141–158.

Larsson, J., Kawai, S., Bodart, J., Bermejo-Moreno, I., 2016. Large eddy simulation with modeled wall-stress: recent progress and future directions. Mech. Eng. Rev. 3 (1), 15–00418.

Larsson, J., Wang, Q., 2014. The prospect of using large eddy and detached eddy simulations in engineering design, and the research required to get there. Phil. Trans. R. Soc. A 372 (2022), 20130329.

Le Ribault, C., Le Penven, L., Buffat, M., 2006. LES of the compressed Taylor vortex flow using a finite volume/finite element method on unstructured grids. Int. J. Numer. Meth. Fluids 52 (4), 355–379.

Lien, F., Chen, W., Leschziner, M., 1996. Low-Reynolds-number eddy-viscosity modelling based on non-linear stress-strain/vorticity relations. Eng. Turbul. Modell. Exp. 3 (1), 91–100.

Ma, P., Ewan, T., Jainski, C., Lu, L., Dreizler, A., Sick, V., Ihme, M., 2017a. Development and analysis of wall models for internal combustion engine simulations using high-speed micro-PIV measurements. Flow Turbul. Combust. 98, 283–309.

Ma, P., Greene, M., Sick, V., Ihme, M., 2017b. Non-equilibrium wall-modeling for internal combustion engine simulations with wall heat transfer. Int. J. Engine Res. 18 (1-2), 15–25.

Mandanis, C., Schmitt, M., Koch, J., Wright, Y. M., Boulouchos, K., 2017. Wall heat flux and thermal stratification investigations during the compression stroke of an engine-like geometry: A comparison between LES and DNS. Flow Turbul. Combust., doi: https://doi.org/10.1007/s10494-017-9879-x.

Mason, P., Callen, N., 1986. On the magnitude of the subgrid-scale eddy coefficient in large-eddy simulations of turbulent channel flow. J. Fluid Mech. 162, 439–462.

Misdariis, A., Vermorel, O., Poinsot, T., 2015. LES of knocking in engines using dual heat transfer and two-step reduced schemes. Combust. Flame 162, 4304–4312.

Montorfano, A., Piscaglia, F., Schmitt, M., Wright, Y., Frouzakis, C., Tomboulides, A., Boulouchos, K., Onorati, A., 2015. Comparison of direct and large eddy simulations of the turbulent flow in a valve/piston assembly. Flow Turbul. Combust. 95, 461–480.

Morse, A., Whitelaw, J., Yianneskis, M., 1979. Turbulent flow measurements by laser-doppler anemometry in motored piston-cylinder assemblies. J. Fluids Eng. 101 (2), 208–216.

Nguyen, T. M., Proch, F., Wlokas, I., Kempf, A. M., 2016. Large eddy simulation of an internal combustion engine using an efficient immersed boundary technique. Flow Turbul. Combust. 97, 191–230.

Nicoud, F., Toda, H., Cabrit, O., Bose, S., Lee, J., 2011. Using singular values to build a subgrid-scale model for large eddy simulations. Phys. Fluids 23 (085106).

Nuutinen, M., Kaario, O., Vuorinen, V., Nwosu, P., Larmi, M., 2014. Imbalance wall functions with density and material property variations effects applied to engine heat transfer computational fluid dynamics simulations. Int. J. Engine Res. 15 (3), 307–324.

Park, G. I., Moin, P., 2014. An improved dynamic non-equilibrium wall-model for large eddy simulation. Phys. Fluids 26 (1), 37–48.

Piomelli, U., 2008. Wall-layer models for large-eddy simulations. Prog. Aerospace Sci. 44 (6), 437–446.

Piomelli, U., Balaras, E., Pasinato, H., Squires, K., Spalart, P., 2003. The inner–outer layer interface in large-eddy simulations with wall-layer models. Int. J. Heat Fluid Flow 24 (4), 538–550.

Plensgaard, C., 2013. Improved engine wall models for large eddy simulation (LES). Ph.D. thesis, University of Wisconsin-Madison.

Plensgaard, C., Rutland, C., 2013. Improved engine wall models for large eddy simulation. SAE Technical Paper 2013-01-1097.

Pope, S., 2004. Ten questions concerning the large-eddy simulation of turbulent flows. New J. Phys. 6, 1–24.

Popovac, M., Hanjalic, K., 2007. Compound wall treatment for RANS computation of complex turbulent flows and heat transfer. Flow Turbul. Combust. 78, 177–202.

Reitz, R., 2013. Directions in internal combustion engine research. Combust. Flame 160, 1–8.

Renaud, A., Ding, C.-P., Jakirlic, S., Dreizler, A., Böhm, B., 2018. Experimental characterization of the velocity boundary layer in a motored IC engine. Int. J. Heat Fluid Flow 71, 366–377.

Rieth, M., Proch, F., Stein, O., Pettit, M., Kempf, A., 2014. Comparison of the Sigma and Smagorinsky LES models for grid generated turbulence and a channel flow. Comput. Fluids 99, 172–181.

Rutland, C., 2011. Large-eddy simulations for internal combustion engines - a review. Int. J. Engine Res. 12, 421–451.

Sagaut, P., Deck, S., Terracol, M., 2013. Multiscale and multiresolution approaches in turbulence, 2nd Edition. Imperial College Press.

Schiffmann, P., Gupta, S., Reuss, D., Sick, V., Yang, X., Kuo, T., 2016. TCC-III engine benchmark for large-eddy simulation of IC engine flows. Oil Gas Sci. Technol. 71 (1).

Schmitt, M., Boulouchos, K., 2016. Role of the intake generated thermal stratification on the temperature distribution at top dead center of the compression stroke. Int. J. Engine Res. 17 (8), 836–845.

Schmitt, M., Frouzakis, C., Wright, Y., Tomboulides, A., Boulouchos, K., 2014a. Investigation of cycle-to-cycle variations in an engine-like geometry. Phys. Fluids 26 (12), 125104.

Schmitt, M., Frouzakis, C., Wright, Y., Tomboulides, A., Boulouchos, K., 2015a. Direct numerical simulation of the compression stroke under engine-relevant conditions: Evolution of the velocity and thermal boundary layers. Int. J. Heat Mass Transfer 91, 948–960.

Schmitt, M., Frouzakis, C., Wright, Y., Tomboulides, A., Boulouchos, K., 2016a. Investigation of wall heat transfer and thermal stratification under engine-relevant conditions using DNS. Int. J. Engine Res. 17 (1), 63–75.

Schmitt, M., Frouzakis, C. E., Tomboulides, A. G., Wright, Y. M., Boulouchos, K., 2014b. Direct numerical simulation of multiple cycles in a valve/piston assembly. Phys. Fluids 26 (3), 035105.

Schmitt, M., Frouzakis, C. E., Tomboulides, A. G., Wright, Y. M., Boulouchos, K., 2015b. Direct numerical simulation of the effect of compression on the flow, temperature and composition under engine-like conditions. Proc. Combust. Inst. 35 (3), 3069–3077.

Schmitt, M., Frouzakis, C. E., Wright, Y. M., Tomboulides, A., Boulouchos, K., 2016b. Direct numerical simulation of the compression stroke under engine relevant conditions: Local wall heat flux distribution. Int. J. Heat Mass Transfer 92, 718–731.

Schmitt, P., Poinsot, T., Schuermans, B., Geigle, K., 2007. Large-eddy simulation and experimental study of heat transfer, nitric oxide emissions and combustion instability in a swirled turbulent high-pressure burner. J. Fluid Mech. 570, 17–46.

Suga, K., Ishibashi, Y., Kuwata, Y., 2013. An analytical wall-function for recirculating and impinging turbulent heat transfer. Int. J. Heat Fluid Flow 41, 45–54.

Temmerman, L., Hadžiabdić, M., Leschziner, M., Hanjalić, K., 2005. A hybrid two-layer URANS–LES approach for large eddy simulation at high Reynolds numbers. Int. J. Heat Fluid Flow 26 (2), 173–190.

Toda, H. B., Cabrit, O., Truffin, K., Bruneaux, G., Nicoud, F., 2014. Assessment of subgrid-scale models with a large-eddy simulation-dedicated experimental database: The pulsatile impinging jet in turbulent cross-flow. Phys. Fluids 26 (7), 075108.

Toledo, M., Le Penven, L., Buffat, M., Cadiou, A., Padilla, J., 2007. Large eddy simulation of the generation and breakdown of a tumbling flow. Int. J. Heat Fluid Flow 28, 113–126.

Trettel, A., Larsson, J., 2016. Mean velocity scaling for compressible wall turbulence with heat transfer. Phys. Fluids 28 (2), 026102.

Truffin, K., Angelberger, C., Richard, S., Pera, C., 2015. Using large-eddy simulation and multivariate analysis to understand the sources of combustion cyclic variability in a spark-ignition engine. Combust. Flame 162 (12), 4371–4390.

Vermorel, O., Richard, S., Colin, O., Angelberger, C., Veynante, D., 2009. Towards the understanding of cyclic variability in a spark ignited engine using multi-cycle LES. Combust. Flame 156, 1525–1541.

Werner, H., Wengle, H., 1991. Large-eddy simulation of turbulent flow over and around a cube in a plate channel. In: Turbulent Shear Flows 8: Selected Papers from the Eighth International Symposium on Turbulent Shear Flows, Munich, Germany.

White, F., 2006. Viscous fluid flow. Vol. 3. McGraw-Hill Higher Education Boston.

Yang, X., Sadique, J., Mittal, R., Meneveau, C., 2015. Integral wall model for large eddy simulations of wall-bounded turbulent flows. Phys. Fluids 27 (2), 025112.

Yang, X. I., Park, G. I., Moin, P., 2017. Log-layer mismatch and modeling of the fluctuating wall stress in wall-modeled large-eddy simulations. Phys. Rev. Fluids 2 (10), 104601.

## Appendix A. 1-D non-equilibrium model implementation

Fig. A.18 displays the structural schematic of the near-wall model while Fig. A.19 describes model workflow between the main grid an the near-wall subgrid. Following Fig. A.18, the wall-tangential flow direction is determined from the main grid solution and the local $x$-axis is set to be parallel to this velocity. Subscripts $w$, $c$, $h$, and $2c$ henceforth correspond to wall, first cell centre, cell face, and second cell centre values, respectively, while filtering notations in addition to modelled $k$ and $\varepsilon$ subscripts are dismissed for clarity. The cell face quantities $\tau_h = ([\mu + \mu_{mod}]du/dy)_h$ and $q_h = (c_p[\mu/\Pr + \mu_{mod}/\Pr_{mod}]dT/dy)_h$ are evaluated from the main grid data. After initialisation of $\tau_w$ and $q_w$, (e.g. via standard wall functions), variables are scaled as follows:

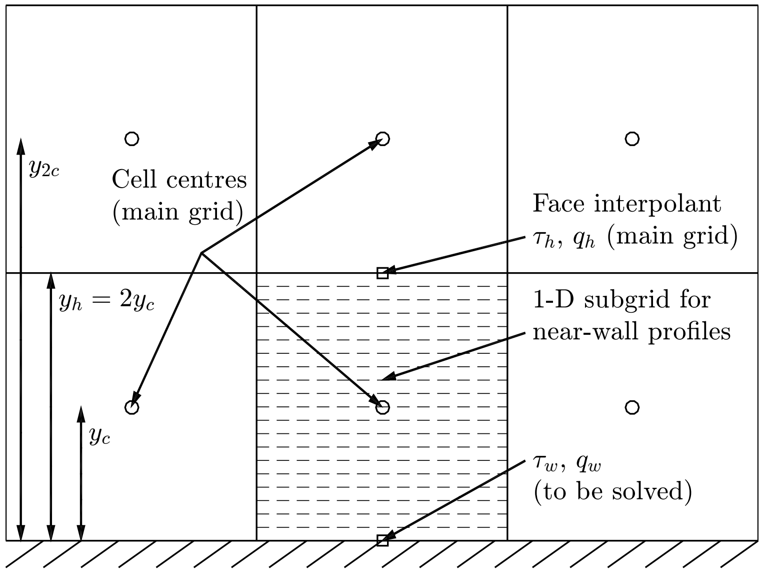


Figure A.18: A schematic description of the wall treatment applied here (HLR-WT) and first published by Nuutinen et al. (2014). Subscripts $w$, $c$, $h$, and $2c$ correspond to wall, first cell centre, cell face, and second cell centre values, respectively.

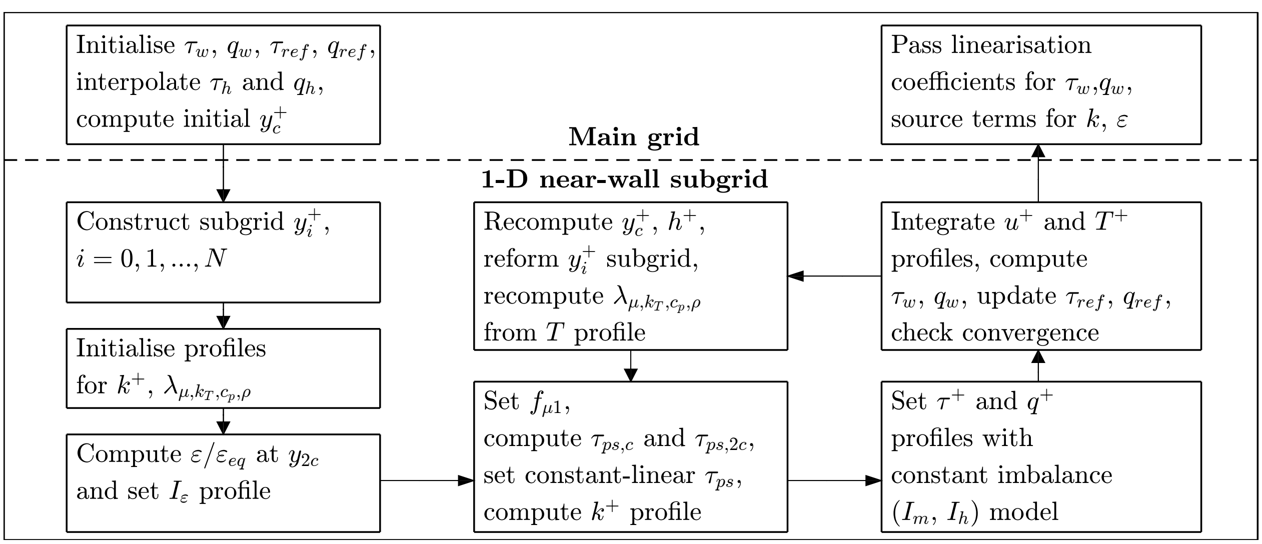


Figure A.19: Workflow chart of the wall treatment between the main grid and the 1-D subgrid.

$$
\begin{array}{lll}
y^+ = \rho_c u_\tau y/\mu_c & (\rho\varepsilon)^+ = \rho\varepsilon/(\rho_c^2 u_\tau^4/\mu_c) & k^+ = C_\mu k^{1/2}/u_\tau^2 \\
u^+ = (u - u_w)/u_\tau & T^+ = \rho_c c_{p,c} u_\tau (T - T_w)/q_w & \tau^+ = \tau_w/\tau_{ref} \\
q^+ = q_w/q_{ref} & &
\end{array}
\tag{A.1}
$$

where the shear velocity $u_\tau = (\tau_{ref}/\rho_c)^{1/2}$ and the 'reference' wall shear stress and heat flux values ($\tau_{ref} = \tau_w + \tau_{small}$, $q_{ref} = q_w + q_{small}$) have been introduced to avoid zero division. The initial subgrid $y_i^+$ $(i = 0, 1, ..., N)$ is then constructed. To describe subgrid material property variation, scaled profiles $\lambda_\mu$, $\lambda_{k_T}$, $\lambda_{c_p}$, $\lambda_\rho$ denote $\mu/\mu_c$, $k_T/k_{T,c}$, $c_p/c_{p,c}$ and $\rho/\rho_c$, respectively. The profiles are approximated with power laws, e.g. for viscosity:

$$
\lambda_\mu = \frac{\mu}{\mu_c} = \left(\frac{T}{T_c}\right)^\Phi \tag{A.2}
$$

wherein the exponent is obtained from the reference values, i.e. $\Phi = \ln(\mu_w/\mu_c)/\ln(T_w/T_c)$. The reference values (at cell centres and walls) are computed by Star-CD internally using more complex models. The power law exponents are estimated similarly for other quantities, with the exception of density, where $\Phi = -1$ due to the ideal gas law.

After initialising $\lambda_{\mu,k_T,c_p,\rho} = 1$, a dissipation rate imbalance profile $I_\varepsilon$ is computed according to a linear profile between $I_{\varepsilon,w} = 1$ and $I_{\varepsilon,2c} = \varepsilon(y_{2c})/\varepsilon_{eq}(y_{2c})$. Here, $\varepsilon = (\varepsilon_{iso} + \varepsilon_{wall})I_\varepsilon$ where isotropic dissipation $\varepsilon_{iso} = C_\mu^{3/4} k^{3/2}/(\kappa y)$, wall dissipation $\varepsilon_{wall} = 2\nu(k/y^2)g_\varepsilon$ and $\varepsilon_{eq} = \varepsilon_{iso} + \varepsilon_{wall}$ is the equilibrium form. The shape function $g_\varepsilon = 1 - (y^*/\delta_\varepsilon)\exp(-\chi_\varepsilon y^*/2\delta_\varepsilon)$ (where $\delta_\varepsilon = 3.31$, $\chi_\varepsilon = 0.75$, $y^* = \rho C_\mu^{1/4} k(y/\mu)$) is set to cancel near-wall diffusion of $k$ (exactly at the wall). The damping function profile is computed nondimensionally as $f_{\mu1}^+ = 1 - \beta_\mu \exp(-\alpha_\mu[\lambda_\rho/\lambda_\mu]k^{+1/2} y^+)$. $\beta_\mu = 1 - (\rho\varepsilon)_w^+ C_\mu^{1/2}/(2\kappa^2) = 0.7864$ has been calibrated for a realistic (non-zero) wall dissipation level $(\rho\varepsilon)_w^+ = 0.25$ on the basis of DNS studies (Iwamoto et al., 2002a,b) while $\alpha_\mu = 0.011857$ is set to asymptotically match standard wall functions in ideal conditions. A corrected $k^+$ profile is generated utilising a pseudo-stress $\tau_{ps}$

$$
\tau_{ps} = \frac{I_\varepsilon C_\mu^{1/4} k^{1/2}(\mu + \mu_{mod})}{\kappa y f_{\mu1}^{1/2}} \tag{A.3}
$$

whereby a constant value $\tau_{ps,c}$ is set for the interval $y = [0, y_c]$ while a linear variation from

$\tau_{ps,c}$ to $\tau_{ps,h}$ (based on $\tau_{ps,2c}$) is set between $y = [y_c, y_h]$. Thereafter, an updated $k^+$ profile is computed

$$k^+ = \left( \frac{2\kappa y^+ {f_{\mu 1}^+}^{1/2} \tau_{ps}^+ / I_\varepsilon}{\lambda_\mu + [\lambda_\mu^2 + 4\lambda_\rho \kappa^2 {y^+}^2 {f_{\mu 1}^+}^{3/2} \tau_{ps}^+ / I_\varepsilon]^{1/2}} \right)^2 \tag{A.4}$$

where $\tau_{ps}^+ = \tau_{ps}/\tau_{ref}$. Eqs. (15)-(16) are expressed nondimensionally as

$$\frac{du^+}{dy^+} = \frac{\tau^+}{\lambda_\mu + \lambda_\rho \kappa y^+ {k^+}^{1/2} f_{\mu 1}^+ / I_\varepsilon} \tag{A.5}$$

$$\frac{dT^+}{dy^+} = \frac{Pr_c Pr_{mod} q^+}{Pr_{mod} \lambda_{k_T} + Pr_c \lambda_{c_p} \lambda_\rho \kappa y^+ {k^+}^{1/2} f_{\mu 1}^+ / I_\varepsilon} \tag{A.6}$$

where the modelled Prandtl number $\mathrm{Pr}_{mod} = 0.9\left(1 - \exp[-\gamma\sqrt{y^+}]\right)$ and $\gamma = 0.9470$. Eqs. (A.5) and (A.6) are numerically integrated to yield the velocity and temperature profiles – here, scaled $\tau^+$ and $q^+$ profiles are linear similarly to Eqs. (15) and (16):

$$\tau^+ = \frac{\tau_w + (\tau_h - \tau_w)(y^+/h^+)}{\tau_{ref}} \qquad q^+ = \frac{q_w + (q_h - q_w)(y^+/h^+)}{q_{ref}} \tag{A.7}$$

Finally, wall fluxes are computed for the next iterative step $n+1$ (or, after convergence of $u^+$ and $T^+$, to the main grid) in linearised form as

$$\tau_w^{n+1} = \overbrace{\left( \left[ \frac{\tau_w}{\tau_{ref}} \frac{y_c^+}{u_c^+} \right] \frac{\mu_c}{y_c} \right)}^{lin.coeff.} (u_c - u_w) \tag{A.8}$$

$$q_w^{n+1} = \overbrace{\left( \left[ \frac{q_w}{q_{ref}} \frac{y_c^+}{T_c^+} \right] \frac{c_{p,c}\mu_c}{y_c} \right)}^{lin.coeff.} (T_c - T_w) \tag{A.9}$$

For the next iterative step, updated material properties are computed based on the temperature profile, while the subgrid $y_i^+$ is modified based on the updated wall shear stress value. Modelled turbulence source terms are provided as

$$\langle \rho P_k \rangle = \left\langle \rho P_{k,tan}^{nw} \right\rangle + \left( \rho P_k^{main} - \rho P_{k,tan}^{main} \right) \tag{A.10}$$

$$\langle \rho \varepsilon \rangle = \frac{\langle (\rho\varepsilon)^+ \rangle}{(\rho\varepsilon)_c^+} \varepsilon_{eq,c} I_{\varepsilon,c} \tag{A.11}$$

where angled brackets denote averaging over the near-wall subgrid. The near-wall tangential production is obtained as

$$\left\langle \rho P^{nw}_{k,tan} \right\rangle = \left\langle \lambda_\rho \kappa y^+ {k^+}^{1/2} f^+_{\mu 1} (du^+/dy^+)^2 / I_\varepsilon \right\rangle (\rho_c^2 u_\tau^4 / \mu_c) \tag{A.12}$$

## Appendix B. Preliminary cycle selection criteria

From the results of Stage I computations, a nominal cycle (A) is determined in addition to two differing cycles (B and C). Cycles are determined based on mean axial flow profiles at 90°CA ATDC (Fig. 5) so that A is the cycle closest to the mean statistical cycle, B is farthest from A, and C is farthest from B. This procedure utilises the following metric:

$$M_{cn} = \sum_i \sum_j \left| r_j \left( \langle \tilde{u}_z(r_j, z_i) \rangle_{\phi,cn} - u_{z,ref} \right) \right| \tag{B.1}$$

where $cn$ is the cycle number and $\langle \cdot \rangle_{\phi,cn}$ signifies instantaneous azimuthal averaging within the selected cycle. Summation is carried out over equally spaced radial points $r_j$ located at axial planes $z_i = [-10, -20, \ldots, -50]$ mm and $u_{z,ref}$ is a reference profile set. Profile differences are radially weighted to ensure equivalence in axial momentum contribution.

For the determination of nominal cycle A, a minimum of $M_{cn}$ is probed with respect to the statistical mean cycle ($u_{z,ref} = \langle \tilde{u}_z \rangle$ where $\langle \cdot \rangle$ denotes averaging over both the azimuthal coordinate and all of the 17 considered cycles). For cycle B, a maximum of $M_{cn}$ is sought with the azimuthally averaged cycle A as the reference ($u_{z,ref} = \langle \tilde{u}_z \rangle_{\phi,A}$) whereas for determining cycle C, a maximum of $M_{cn}$ is determined with cycle B as the reference.